Satellite-based evidence of regional and seasonal Arctic cooling by brighter and wetter clouds

Luca Lelli[1,2], Marco Vountas[1], Narges Khosravi[3], and John P. Burrows[1]

[1]Institute of Environmental Physics and Remote Sensing, University of Bremen, Germany
[2]NASA Goddard Space Flight Center, Greenbelt, MD, USA
[3]Alfred-Wegener-Institut, Bremerhaven, Germany

Correspondence: Luca Lelli (luca@iup.physik.uni-bremen.de)

Abstract. Using two decades of satellite-based measurements of reflectance of solar radiation at the top-of-atmosphere and a complementary record of cloud properties, it is concluded that the loss of Arctic brightness due to sea ice retreat is not compensated by a pan-Arctic increase in cloudiness, but rather by a systematic change in the thermodynamic phase of cloud and a resultant effect on cloud reflectance. Liquid water content of the clouds has increased resulting in positive trends in

5   susceptible cloud properties. Consequently, a cooling trend by clouds is superimposed on top of the pan-Arctic amplified warming, induced by the anthropogenic release of greenhouse gases, the ice albedo feedback and related effects. Except above the permanent and marginal sea ice zone around the Arctic circle, the rate of surface cooling by clouds has increased, both in spring (-32% in total radiative forcing for the whole Arctic) and in summer (-14%). The magnitude of this effect depends on both the underlying surface type and changes in the regional Arctic climate.

10 **1 Introduction**

The most recent climate projections indicate that the Arctic will be free of sea ice by the summer of 2035 (Guarino et al., 2020). The Arctic near-surface increase of temperatures is about twice the global average over the past four decades. This is referred to as "Arctic Amplification" (Serreze and Francis, 2006). The size of a temperature increase from a doubling of the carbon dioxide atmospheric loading was first quantified by Arrhenius in 1896 (Arrhenius, 1896). The impact of the anthropogenic

15 release of greenhouse gases on the surface temperature has become an increasingly important topic of scientific interest, pubic debate and concern and international environmental policy, since at least 1990. However, the Arctic is a special case (Serreze and Barry, 2011).

Modeling the changing behavior of clouds sufficiently accurately is identified as the most uncertain factor in the climate projections of greenhouse gas forcing (Zelinka et al., 2020). This is in large part because clouds modulate the Arctic radiation

20 budget in the shortwave (SW) and longwave (LW). . Changes in the temperature, water vapor and the availability of cloud condensation nuclei result in turn in changes in the cloud absorption and reflectance. Thus, improved knowledge of the changing optical and radiative properties of clouds, the Earth's surface and the resultant SW reflection and LW emission at the top of the atmosphere are essential to test and improve the accuracy of climate model projections. The most complex and ambitious measurement endeavours (Wendisch et al., 2019; Shupe et al., 2021), exploiting the synergy of on-ground, ship and airborne

25 techniques, rely on complementary measurements of satellite sensors which provide synoptic coverage of the Arctic clouds over long time scales.

Instruments aboard satellites measure the solar radiation scattered back to space from the Arctic surface and atmosphere constituents (i.e. ice, snow, ocean, land, clouds, trace gases and aerosols (Kokhanovsky and Tomasi, 2020; Serreze and Barry, 2014)). Each contribution has a different response to radiation depending on their physical properties. Incoming solar SW

30 radiation in the ultraviolet and visible is scattered strongly by ice, snow, and clouds, whereas open waters absorb significantly and scatter back to space much less electromagnetic radiation in the solar spectral range. On the other hand, LW radiation fluxes are also modulated by clouds, which may warm or cool both the Top-Of-Atmosphere (TOA) and the surface. The changes at the surface resulting from the interplay of changes in sea ice properties, snow and cloud properties in the atmosphere lead to a nonlinear response of the radiation budget in the Arctic to changes in temperature (Lindsay and Zhang, 2005).

35 Cloud fractional cover (CFC) over the Arctic can be as large 70% throughout the year (Karlsson and Devasthale, 2018). The magnitude and variability of CFC depends on atmospheric conditions, which impact on cloud nucleation and growth, and on the type of sensors used to measure it (Chan and Comiso, 2013). The CFC seasonal cycle exhibits a strong bimodal distribution, with a maximum up to 90% in summer along the North Atlantic throughout the circumpolar ocean waters and a minimum of 40% in winter months (Eastman and Warren, 2010b, a; Boccolari and Parmiggiani, 2018). Rather than having a

40 latitudinal dependence, CFC in the Arctic appears to be dependent on the underlying surface type, meteorology and topography. Distinct patterns having divergent CFC trends and types in the Arctic have been identified, which follow sea ice and open waters contours. Using the same data sets does not guarantee consistent analysis and interpretation of the observations. This is the case for Boccolari and Parmiggiani (2018), where CFC data, derived from AVHRR (see Tab. A1 for the meaning of all acronyms) over the Arctic between 1982 and 2009, is in unexpected and large disagreement with results from Schweiger (2004) and Wang

45 and Key (2005b), even though all three research groups use the same data.

Clouds are the most important atmospheric factor in the modulation of energy flow exchange between the Arctic and its surroundings. Sledd and L'Ecuyer (2019) partitions the relative importance of surface and atmosphere with respect to the changes of albedo at TOA. While the majority of the variability is controlled by surface reflection, TOA albedos are consistently influenced by radiative transfer in the atmosphere: the contribution of the atmospheric reflection being approximately 84% of

50 the total Arctic albedo. This finding is relevant for a melting cryosphere, in which the relative changes in surface reflection are offset by atmospheric reflection, primarily by the reflectance of clouds (Donohoe and Battisti, 2011). Consequently and as expected, the presence of clouds limits the impact of the changes of the surface reflectance on the spectral reflectance at TOA (R_λ^{TOA}). Hence, a decrease in summer CFC over Greenland is held responsible for the ice mass loss acceleration and, consequently, for the decrease in albedo. A decrease in cloudiness implies an increase of SW downwelling fluxes at the surface.

55 This is correlated with the synoptic North Atlantic Oscillation (Hofer et al., 2017) and anticyclonic activity promoting adiabatic tropospheric warming of subsiding air masses (Shahi et al., 2020).

In Pistone et al. (2014) a downward trend of all-sky albedo across the Arctic is reported. This is not compensated by an opposite trend in cloudiness, thus levelling out the recent pan-Arctic reflectance trend. However, this analysis is limited to oceanic regions and additional uncertainties are caused by the conversion from clear-sky to all-sky albedo at the beginning of

60 their record. As the clear-sky signal is derived from the sea-ice record with sensors for which the atmosphere is almost entirely transparent, the all-sky albedo is computed with a post-hoc method adding the atmospheric part and is not the outcome of direct satellite measurements. He et al. (2019) reports significant regional covariance of CFC and sea ice. Strong negative correlations are seen over Beaufort and East Siberian Seas. The highest CFC occurs typically over marginal sea ice regions. The latter is negatively correlated with sea ice anomalies. The magnitude of the surface albedo feedback is limited by the formation of

65 low-level clouds from the evaporation of the melted sea ice regions. In such conditions, clouds have a negative feedback, in the SW radiation spectral region. This offsets LW radiation emission. Overall, He et al. (2019) consider that CFC over the melted water influences the albedo change in the albedo feedback process. The extra CFC resulting from sea ice loss is a second-order contribution.

The feedback mechanisms associated with the increase in surface absorption of solar radiation are often cited as the main

70 contributor to the loss of ice and snow in the Arctic (Serreze and Francis, 2006; Crook et al., 2011). However, Pithan and Mauritsen (2014) proposes that temperature-related processes dominate the Arctic warming. Temperature rise influences cloud formation and precipitation (Herman and Goody, 1976; Curry et al., 1996), which amplify warming in the Arctic region (Taylor et al., 2013), although there are disagreements on the impact of clouds in this respect. For instance Screen and Simmonds (2010) reported that changes in CFC do not strongly contribute to the Arctic Amplification despite their role in "enhanced warming in

75 the lower part of the atmosphere during summer and early autumn", whereas Francis and Hunter (2006) relate the loss rate of the the perennial sea ice edge shelves to CFC and downwelling LW during spring months.

In addition to the warming from the release of greenhouse gases, the dynamics of air masses and physical properties of clouds may contribute to the tropospheric thermal emission. CFC aside, the optical properties of clouds, such as the optical thickness (COT, τ) and effective radius r_{eff} of droplets/crystals, and liquid/ice water content (LWP/IWP), regulate downwelling

80 LW. Model projections of the century ahead show that Arctic clouds during summer are rather unaffected by sea ice variability but their response to sea ice loss is to become optically thicker, have higher LWP, and more frequent low-level liquid phase within the boundary layer (Morrison et al., 2019). Hence, the changes in τ and thermodynamic phase of clouds enhance or suppress cloud radiative forcing (CRF) at the surface. This behavior has been identified in the continuous surface measurements above the Beaufort and Chuckchi Seas (Shupe and Intrieri, 2004), at Ny-Ålesund, Svalbard (Ebell et al., 2019) and in the data

85 products retrieved from AVHRR (Francis and Hunter, 2006).

From the above review of current knowledge about the changing conditions in the Arctic, we consider that investigations of the R_λ^{TOA} and the cloud properties over the past two decades will provide insight into the evolution of the Arctic Amplification.We have prepared a consolidated R_λ^{TOA} data set from 1995 to 2018. A key set of satellite sensors record backscattered radiation in the solar portion of the spectrum. Consequently, this study focuses on the months between April and Septem-

90 ber. The Arctic seasons considered are spring, defined for our purposes as April May June (AMJ) and summer, July August September (JAS) (see App. 2.1). The investigation of R_λ^{TOA} trends involved analysis of the last twenty years of cloud properties from the observations of AVHRR, retrieved with the latest algorithms (Stengel et al., 2020) (see App. 2.2), which supersede older popular data sets, for which specific errors have been found (Zygmuntowska et al., 2012). We build on the heritage of

the earlier studies describing the Arctic state and extend the trend analyses limited previously to 1982–1999 (Wang and Key, 2005b, 2003).

The objectives of this paper are threefold. Firstly, we provide evidence that space-borne measured, spectral R_λ^{TOA} is a valuable indicator of the changing atmospheric composition and surface properties of the Arctic. Secondly, we determine R_λ^{TOA} trends at regional and seasonal scales and reveal unexpected patterns of behavior. Thirdly, we attribute the trends in R_λ^{TOA} to changes in the thermodynamic phase of clouds. Lastly, we quantify the average radiative forcing by clouds and its changes. We relate the latter to the changes in the physical properties of clouds in response to climate change.

2 Data and Methods

The study of the Arctic geophysical domains by remote sensing requires sensors with broad spectral coverage at an adequate spectral resolution to be able to separate different spectral features of gases, surfaces, liquid water and ice/snow. We define the spectral reflectance measured at TOA - R_λ^{TOA} - as

$$R_\lambda^{\mathrm{TOA}} = \frac{\pi I_\lambda}{\cos(\theta_0)\, E_\lambda^0}, \tag{1}$$

where I_λ is the Earthshine, i.e. the upwelling scalar radiance measured at TOA (units of photons $\times$ s^{-1} cm^{-2} nm^{-1} sr^{-1}), E_λ^0 the unpolarized downwelling solar irradiance (photons $\times$ s^{-1} cm^{-2} nm^{-1}) and θ_0 the solar zenith angle in degrees.

Relevant parameters for the R_λ^{TOA} analysis are shown in Fig. 1. The left y-axis of Fig. 1-a shows I_λ, E_λ^0 for a GOME measurement above the Kara Sea, while the right y-axis shows modeled R_λ^{TOA}, in satellite perspective, representing the TOA signal for typical Arctic geophysical conditions. Fig. 1-b shows the wavelength dependence, at GOME spectral resolution, of the spectral reflectance for different surface types. The almost flat Earthshine between 450–800 nm reveals the presence of a cloud deck or snow surface in the satellite field of view. Ten wavelength bands of spectral width 5-10 nm have been selected satisfying the following requirements: they are chosen to be similar to those of sensors' channels used in the literature for comparative purposes. Their coverage from the UV to the NIR shall provide differential sensitivity to individual components of the Arctic atmosphere-surface. Additionally, they should exclude strong absorption by atmospheric trace gases to avoid misinterpretation of the observed behavior. Two exceptions are the broadband O$_3$ Chappuis band (525–675 nm) and the narrow O$_2$ A-band (centred at 760 nm). The former, even if smoothed at 5-10 nm resolution, has information on the total column of ozone and on the structure of the upper troposphere and lower stratosphere. Well-mixed gas, such as oxygen, provide valuable diagnostics about the depth of the atmospheric column, as seen from space. The A-band is used to assess the surface topography in a cloud-free atmosphere (van Diedenhoven et al., 2005) and altitude, geometrical and optical depth of clouds over dark (Rozanov and Kokhanovsky, 2004; Lelli et al., 2012, 2014) and bright (Schlundt et al., 2013) surfaces.

2.1 Reflectance data

To detect changes on daily, monthly, seasonal and decadal scales several measurements per day of adequate spatial resolution must be made over several decades. The polar-orbiting spectrometer suite comprising GOME, SCIAMACHY and GOME-2
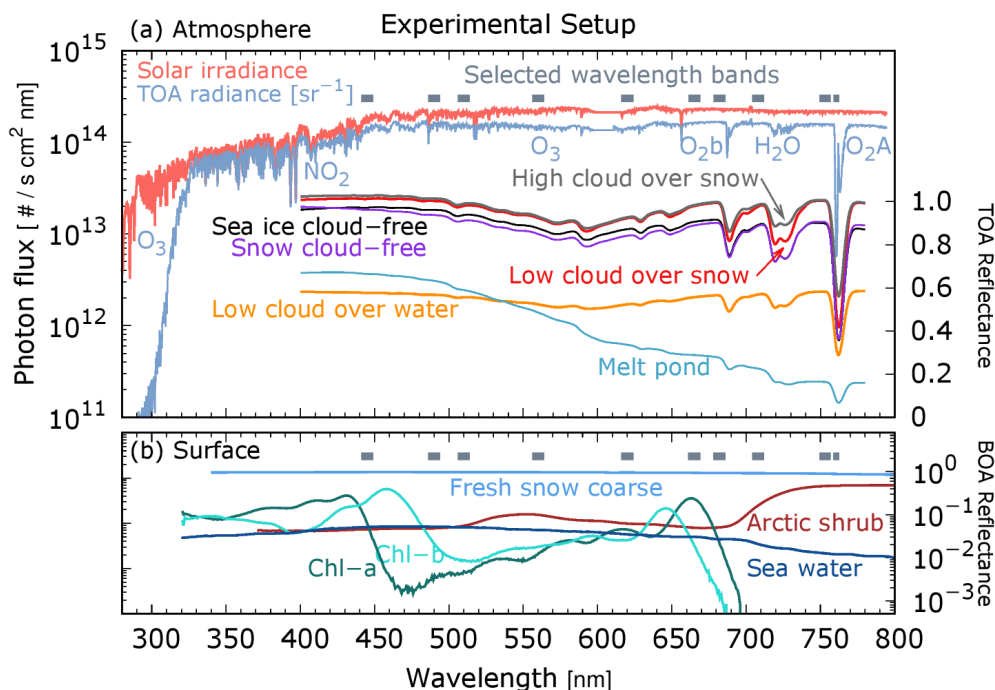
Figure 1. Plots of the solar irradiance, the radiance of a cloud (Earthshine) and reflectances at top (TOA) and bottom (BOA) of the atmosphere as a function of wavelength from 280 nm to 800 nm. The cloud radiance was observed by GOME on May 15, 2001 over Kara Sea (80.53°N, 75.99°E). Modelled R_λ^{TOA} (nadir, solar zenith 40°) display a water cloud, placed at 3 km and optically dense 30, above sea water and snow, with a cloud-free sea ice, snow and melt pond spectrum. The lower panel shows the black sky hemispherical reflectance at the ground of relevant Arctic surface components. Chlorophyll absorption is taken from Clementson and Wojtasiewicz (2019) and plotted for a May 2016 concentration of 12 mg m^{-3} observed in the Bering Sea (Frey et al., 2018). Arctic shrub and coarse snow data are taken from the ECOSTRESS and ASTER spectral libraries (Meerdink et al., 2019; Baldridge et al., 2009). Melt pond and sea ice albedos are from Istomina et al. (2013).

125 (Tab. A2 for their specifications) is an optimal choice given the individual length of the time series and their high spectral resolution. Description of GOME can be found in Burrows et al. (1999), while SCIAMACHY and GOME-2 are respectively provided in Burrows et al. (1995) and Munro et al. (2016). The detailed steps to harmonize R_λ^{TOA} measured by sensors of different technical specifications are given in the App. A.

Sensors measuring solar radiation scattered back to the top of the atmosphere do not measure at night. Measurements in
130 thermal infrared ($\lambda \gtrsim 4\,\mu\mathrm{m}$) are required to record the thermal emission from the surface and the atmosphere. In practice, this situation, coupled with different sensor swath widths, limits the use of R_λ^{TOA} measurements up to a common north parallel for those months that guarantee adequate sampling. This effect is illustrated plotting the pan-Arctic annual cycle of R_λ^{TOA} in Fig. 2. At the three wavelengths 510, 560, and 760 nm, the seasonality shows that summer months have lower R_λ^{TOA} and higher otherwise. The darkening of the Arctic can also be seen by comparing the years at the beginning of the record, 1996,
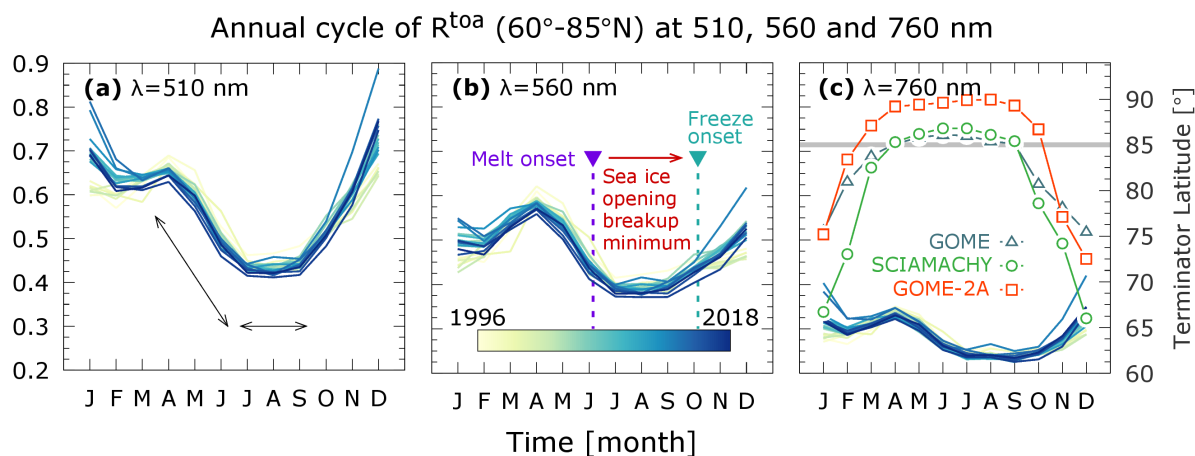
Figure 2. Annual cycle of spectral R^{TOA} at three wavelengths ($\lambda = 510, 560, 760$ nm) for the full record from 1996 to 2018. All sets exhibit the demarcation between months of steep (Apr-May-Jun) and flat gradient of R^{TOA} (Jul-Aug-Sep). This shift leads by one month melt onset (6 Jun), followed by sea ice opening, breakup, minimum (16 Jul – Sep inclusive), and freeze onset (4 Oct) as observed with satellite brightness temperatures (Smith et al., 2020). On the rightmost panel the terminator location of the three sensors with the 85°N (grey line) common threshold used for monthly R^{TOA} aggregation.

with the most recent ones. However, this behavior occurs between April and September. These are the months when the individual terminator of the three sensors reaches the latitude 85°N, this being the spatial threshold of common coverage. For the other months (October to March inclusive) the individual terminators do not guarantee sufficient sampling (Fig. 2-c) and the R_λ^{TOA} curves show that recent years are brighter than those at the beginning of the time series.

From Fig. 2 we identify two distinct behaviors of R^{TOA}. One of steepest decrease, from April to June, and one relatively flat, between July and September. In contrast to the common definition of the climatological seasons, we group April, May, June (AMJ) as Arctic spring and July, August, September (JAS) as Arctic summer. This distinction is explained by the sensors' measurement strategy and by the time-dependent physical processes leading to the transition between high-to-low Arctic reflectance in June to the minimum sea ice extent in September. The changes in surface reflectance between April and May are attributed to snow cover changes and those in June to sea ice changes (Smith et al., 2020). Over water, the timing of such transitions increasingly approaches the summer solstice, which is the day of strongest solar insolation, while it moves further away from it over land (Letterly et al., 2018). It is reasonable to regard this day as a more natural demarcation point between Arctic spring and summer.

2.2 Cloud and flux data

In our study, the R_λ^{TOA} data is complemented by a record of cloud properties and fluxes at TOA and BOA. These are inferred from the afternoon orbit of AVHRR sensors onboard the POES missions. The primary reason for choosing these records is the abundance of studies using these data in the Arctic. This has the required coherent radiometric calibration before the

implementation of individual downstream methodology to assess changes across the Arctic. The cloud and flux records, version 3, are presented by Stengel et al. (2020). The application of the cloud algorithm to MODIS measurements, mimicking AVHRR channels, has shown that the retrieval scheme is well aligned with the reference standards of CloudSat and CALIPSO data for

155 CFC, CTH, COT and liquid thermodynamic phase. While agreeing on the sorting of cloud tops between water and ice phases, higher IWP variability is found as compared to that in the reference DARDAR cloud data products (Delanoë and Hogan, 2010). Aggregated IWP histograms do not differ (Stengel et al., 2015). Version 3 has improved version 2 in terms of precision, accuracy and stability (Stengel et al., 2017). Even more relevant to our purpose is the scheme adopted to calculate cloud properties and broadband fluxes. CFC and optical property retrieval uses a neural network trained on CALIOP data to account

160 for the extent of the underlying bright Arctic surface. CTH has been corrected with CALIOP profiles to account for the depth of light penetration inside a cloud. The retrievals of CTH from all infrared thermal channels are influenced by this effect and yield a radiative cloud top height, lower than the physical cloud top. Broadband fluxes are not derived incorporating reanalysis data but the retrieved cloud properties instead. This is important, because the changes in fluxes are coherently related to changes in the cloud properties. Given the standard notation (all = all-sky, clr = clear-sky, $^+$ = upwelling and $^-$ = downwelling fluxes

165 F), the average long-term relative bias of AVHRR-derived fluxes against CERES ranges from $+2.9\%$ for $F_{SW}^{+,all}$ to -2.7% for $F_{LW}^{+,clr}$. Validation with BSRN measurements in the period 2003–2016 shows that the bias (correlation) for $F_{SW}^{+/-}$ in range $[-6.16,+1.99]\,\mathrm{W\,m^{-2}}$ (0.93/0.99) and $[-3.02,+7.60]\,\mathrm{W\,m^{-2}}$ (0.99/0.99) for $F_{LW}^{+/-}$ (Stengel et al., 2020).

Misclassified cloudy scenes especially over dynamically bright surfaces (i.e. marginal and fractional sea ice zones) impact the calculation of broadband fluxes. This has been already noted in first studies comparing ERBE and AVHRR cloud radiative

170 forcing derived with different scene classification schemes (Li and Leighton, 1991). The conversion of directional radiance, measured at TOA, to irradiance requires the knowledge of the angular light redistribution function of the surface and atmospheric components. If this is not accurately assumed, the irradiance and $F_{SW}^{+/-,clr}$ above reflecting surfaces cannot optimally be calculated. Using the same data of our study, it has been found a low sensitivity of trends in cloud radiative forcing to the biases in cloud properties over surfaces of changing brightness (App. d in Philipp et al., 2020, p. 7499). This confirms the

175 suitability of cloud properties retrieved from AVHRR measurements, classified with active sensor data, for Arctic trend studies.

3 Results

The R_λ^{TOA} time series, measured by GOME, SCIAMACHY and GOME-2A over the Arctic region (60–85°N), anomalies, trends and significance were harmonized (for more details see App. A and App. B). They are shown for wavelengths 510, 560 and 620 nm in Figs. 3 and 4. The R_λ^{TOA} retrieved from the sensors MERIS (on Envisat) and GOME-2B (on MetOp-B) confirm

180 that the correction scheme is successful. A consistent and consolidated data set results from the measurements of the three instruments. Any errors are minimized, when sunlight availability across the Arctic provides full coverage for the sensors' swath at highest latitudes. Seasonality is the dominant feature of Fig. 3. Maximum R_λ^{TOA} occurs in early AMJ when the Polar day results in the Arctic being fully illuminated and the ice extent is close to its maximum. Analogously, minimum R_λ^{TOA} occurs from August to September when the days are shortening and sea ice coverage is at its minimum. The observed seasonal cycle
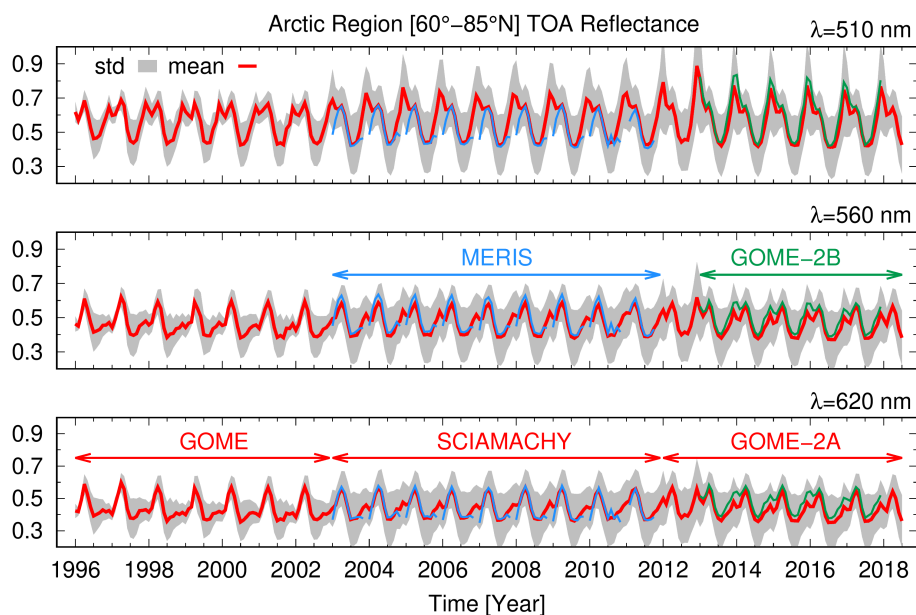
Figure 3. Time series of mean absolute R^{TOA} (red lines) and standard deviation (shaded grey) for the three wavelength bands 510, 560 and 620 nm derived from measurements of GOME, SCIAMACHY and GOME-2A over the Arctic Circle. The companion sensors MERIS on board Envisat (blue) and GOME-2B onboard MetOp-B (green) have been superimposed for comparison.

of R_λ^{TOA} agrees with that observed by models as do the observations of sea ice extent over the Arctic (Holland et al., 2008). This provides evidence to confirm that one dominant parameter in R_λ^{TOA} variability is surface reflectance (Sledd and L'Ecuyer, 2019).

A small downward trend of R_λ^{TOA} for the three wavelengths in the solar range is seen in the anomalies of Fig. 4. The anomaly of R_λ^{TOA} is the difference between the value of R_λ^{TOA} and the climatological average value of R_λ^{TOA} at time t (see App. B). In a warming Arctic a significant decrease in reflectance would have been expected due to sea ice loss. For water and ice-covered regions of the Arctic, Pistone et al. (2014) and Morrison et al. (2019) state that no significant relationship between CFC patterns and sea-ice loss is observed during summer but some is identified in autumn months. Such changes are not observable in the pan-Arctic R^{TOA} anomalies. Rather, the reduction in reflectance is small and not attributable to a specific season. As a consequence, we need to ask whether the loss of reflectance associated with sea ice reduction is compensated by increasing CFC or brighter clouds and which processes lead to the small pan-Arctic R^{TOA} trends.

To answer these questions in the following, we map R_λ^{TOA} in the Arctic, gridded at $1° \times 1.5°$ latitude and longitude. Fig. 5 shows the spatially resolved R_λ^{TOA} trends for $\lambda = 510, 560, 620$ nm over the Arctic region for AMJ and JAS. Similarly, Fig. 6 shows trends for the analyzed wavelengths for the 12 Arctic regions, that are defined using the geographical subdivision proposed by Serreze and Barry (2014) and Wang and Key (2005a) (see Fig. B1). Trends for AMJ are shown in green and the JAS trends for selected spectral bands are shown in blue. The red symbols show the absolute averages of the R_λ^{TOA} values at the beginning of the record for the respective seasons.
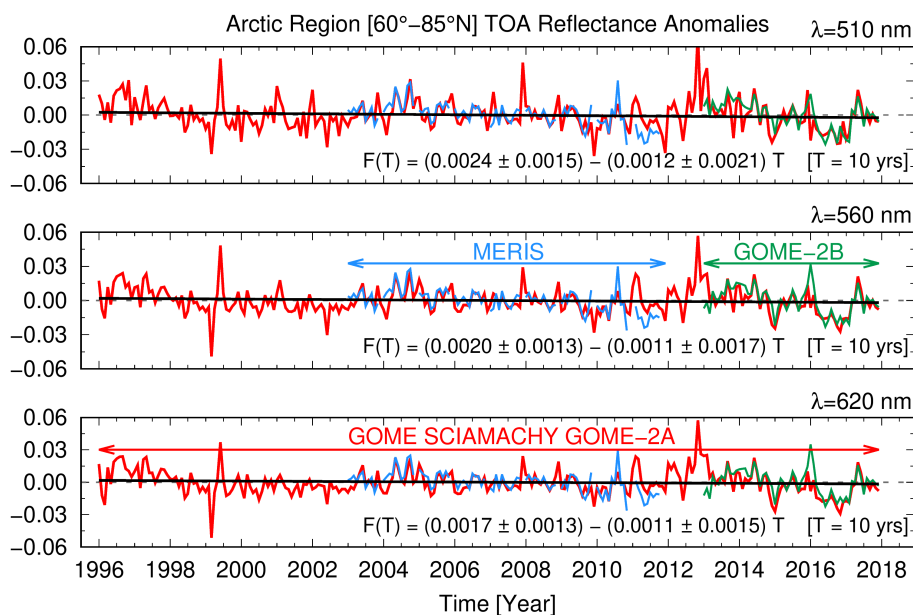
Figure 4. Time series of anomalies of R^{TOA} at $\lambda = 510$, 560 and 620 nm derived from the values of Fig. 3. The values are computed with a seasonal cycle on a sensor basis (see Eq. B1). The linear trend $F(T)$ is shown as black line with the bootstrapped intervals at 95% confidence.

There are marked regional differences. Those that are statistically significant (at 95% confidence level) are shown with red crosses. For AMJ a significant negative trend over the Barents Sea is compensated at all four wavelength bands, by a positive R_λ^{TOA} trend over Greenland, the Canadian Archipelago and Eastern Arctic Seas. In JAS, the negative trend shifts towards areas

205 of the Kara, Laptev and Chuchki Seas. These are Arctic areas having open ocean and are experiencing significant sea ice loss during the period of study. Statistically insignificant increases in R_λ^{TOA} are found over the boreal land masses. However, significant increases in R_λ^{TOA} are observed over Greenland and parts of the Arctic Atlantic sector.

Greenland exhibits positive trends of R_λ^{TOA} in the visible spectrum in both AMJ and JAS. This is not observed in any other region in the Arctic. The result for the Barents Sea is similarly extraordinary. Here the JAS trends of R_λ^{TOA} are strongly negative

210 most likely due to the sea ice loss (Onarheim et al., 2018), but the AMJ result is slightly positive. The values for the most eastern and most western Arctic Seas, i.e. East Siberian Sea, Laptev, Kara, Chuckchi and Beaufort Seas, are often clearly negative for the late summer (JAS) trends, while in AMJ the values show weaker negative or slightly positive trends. Despite its proximity to the Canadian Archipelago, Baffin Bay has changes in R_λ^{TOA} trends that would more closely match the Eastern Arctic Seas region. Over the Hudson Bay, the R_λ^{TOA} trends show unusual patterns. They are largely positive in JAS and relatively strongly

215 negative in AMJ. During JAS the trends for $R^{\text{TOA}} = 760$ nm are large. We infer that this results from a change in clouds, induced by either increased cloud height (CTH), cloud fractional cover (CFC) or albedo (CA).

Although not of the same magnitude, almost all regions show a reflectance change at λ 760 nm. Oxygen absorption is modulated primarily by CTH and, to a lesser extent, by CFC and optical properties such as CA and COT. In this context,
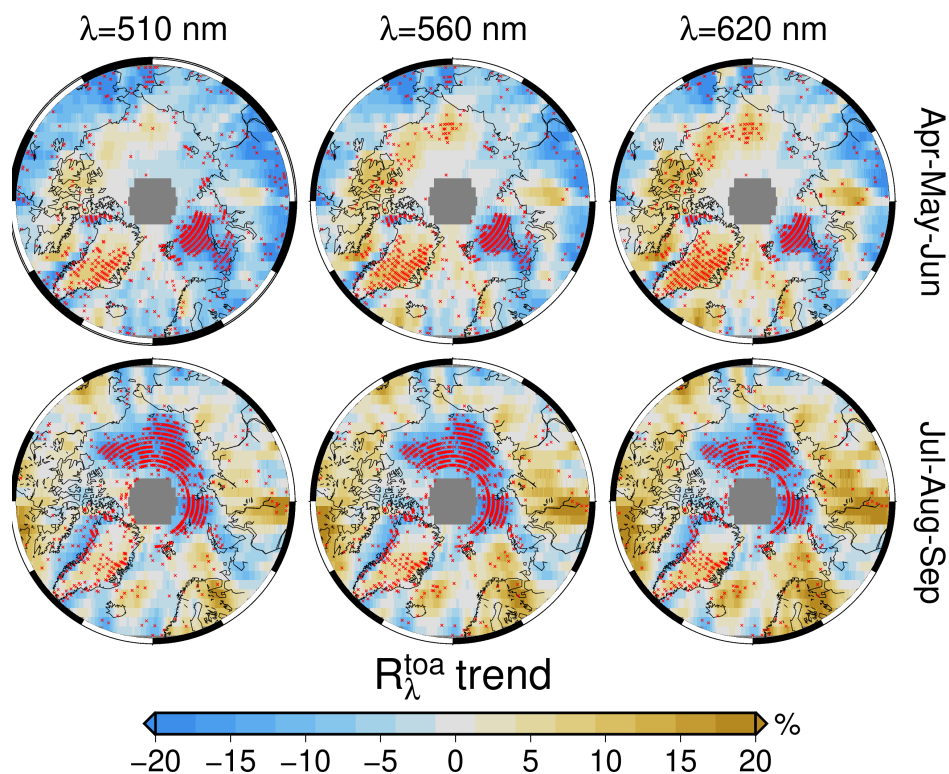
Figure 5. Seasonal R_λ^{TOA} trends for 1996–2018 at selected λ for Arctic spring (AMJ, top) and summer (JAS, bottom). The values are relative to the leading season of the record. Stippling in red indicates significant trends at 95% confidence.

a particularly large number of statistically significant large trend values of R_λ^{TOA} are observed over Greenland during AMJ,
220   which indicate a clear change in occurrence of clouds or one of their scattering properties. Knowing that R^{TOA} is influenced by scattering and absorption in the atmosphere (Sledd and L'Ecuyer, 2019; Donohoe and Battisti, 2011) and that the atmospheric R^{TOA} can be additionally partitioned into cloud, aerosol and gas contributions, this prompted us to examine changes in those cloud properties which directly influence the spectral R^{TOA} trends.

3.1   Cloud properties

225   The globally-validated and consolidated cloud record (Stengel et al., 2020) has first been analyzed across the Arctic (60°– 85°N). The top plot of Fig. 7 shows time series of CFC and CTH. Both parameters show small, statistically insignificant, trends over the last 20 years. CFC has slightly increased by about 0.001 (+0.14%) decade^{-1} while cloud tops are lower by ≈ 6 m (−0.14%) decade^{-1}. This finding obviously excludes an explanation being that reflectance loss at visible wavelengths, due to shrinking sea ice extent, is offset by more CFC or that the loss of CFC reveals more bright underlying surfaces. However,
230   the middle plot of Fig. 7 shows that over two decades the COT temporal trend of liquid clouds has opposite sign of that of cold
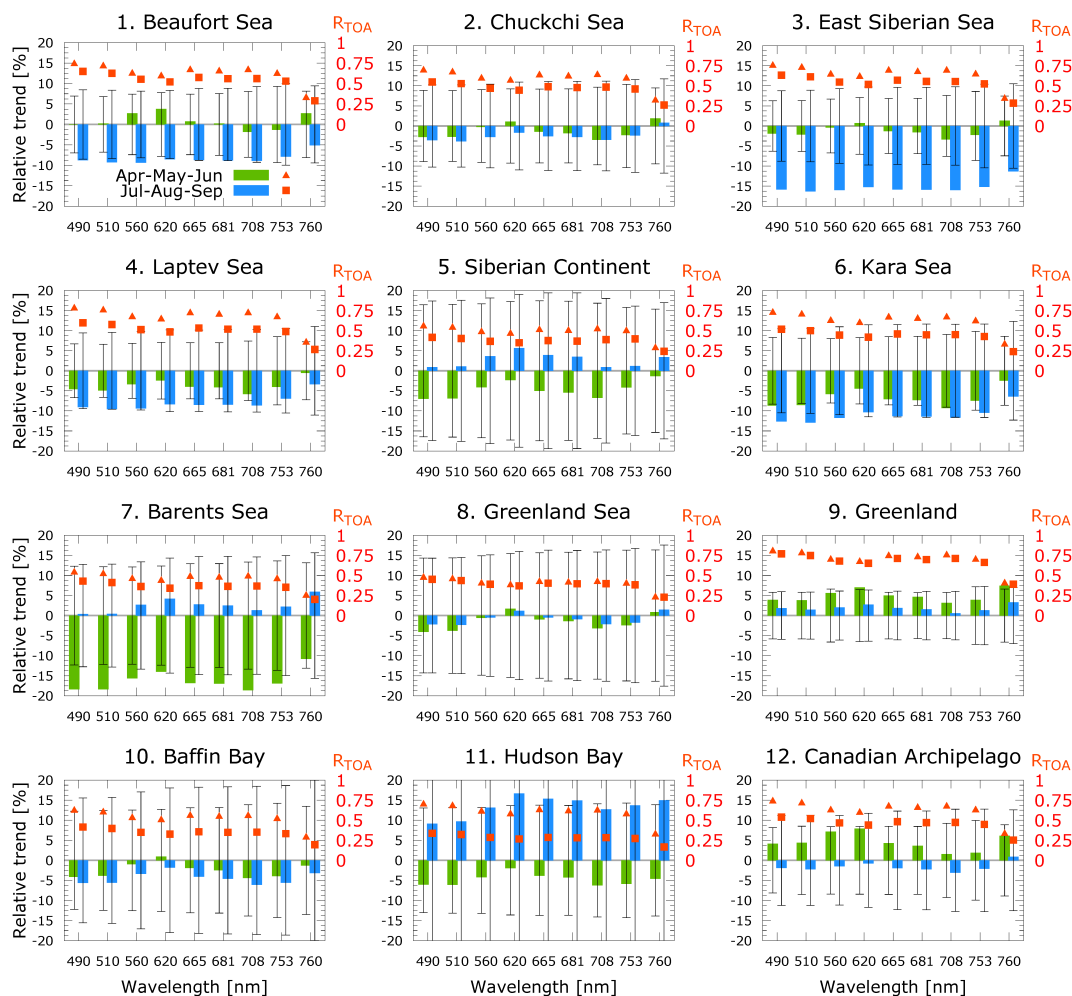
Figure 6. R_λ^{TOA} trends for the twelve regions defined in Fig. B1 for spring (AMJ, green bars) and summer (JAS, blue) months. The secondary y-axis display the absolute mean values of reflectance for each Arctic sector. The trend values are relative to the respective lead season and express the total change throughout the record.

ice clouds. τ of liquid warm clouds increases, statistically significantly, by about 0.4 (+2.85 %) decade^{-1} while the ice-cloud τ decreases by 0.65 (−6.15 %) decade^{-1} in the same period.

Similar to the approach we used for the R_λ^{TOA} trends regionally and qualitatively, we map cloud parameters in the bottom panel of Fig. 7, adding also the albedo of clouds at $\lambda = 600$ nm. CFC trends are regionally partitioned and are seen to increase

235 in the range 5–20 % where the greatest sea ice losses are observed. This occurs during AMJ and less extensively in JAS. Examples of this behavior are found in the Barents, the Kara and Laptev Seas. On the contrary, large areas of statistically significant decrease in the range 2.5–10 % are homogeneously observed across land masses circling the inner polar belt. This includes Greenland and the Atlantic corridor, confirming past results (Hofer et al., 2017). More pronounced trends of the
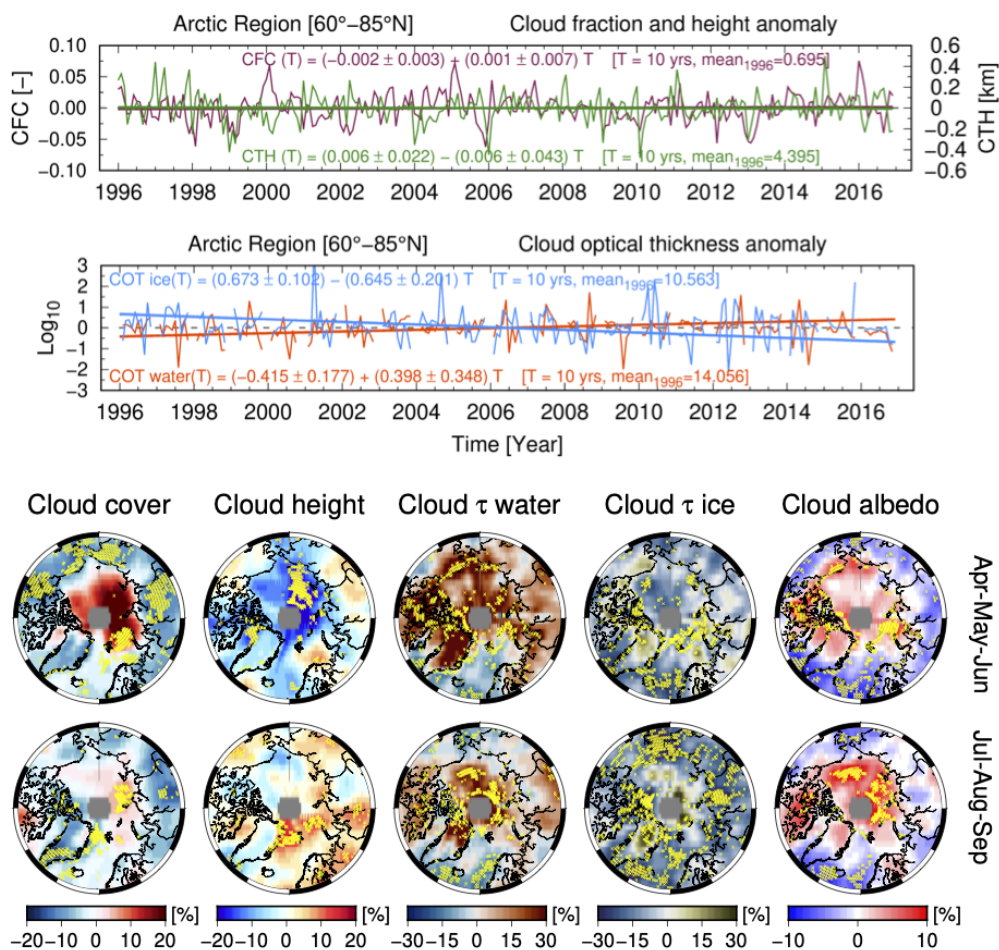
Figure 7. For cloud cover (CFC), height (CTH), optical thickness (COT, τ) of warm liquid and cold ice clouds the left panel shows the pan-Arctic trends, while the right panel shows maps of their seasonal breakdown together with cloud albedo (CA) at λ=600 nm. The trend values in % are relative to the property value at the start year (1996) in the record. Stippling in yellow indicates statistical significance at 95% confidence.

different cloud parameters, irrespective of their sign, occur in AMJ rather than in JAS. The Hudson Bay is one of the few

240   regions experiencing a seasonal trend reversal. The AMJ period is characterized by less cloudiness (-5%), whereas the JAS period exhibits an increase of the order of almost 10% over the last two decades. The resemblance to the trend reversal of all R^{TOA} channels (Fig. 6) indicates that CFC changes primarily modulate R_λ^{TOA} over the Hudson Bay. This is inferred from the absence of change of trend sign of those cloud parameters that influence the reflectance in the solar spectrum, such as COT of water and ice clouds (third and fourth column in Fig. 7).

245   CTH decreases, especially where statistically significant trends are observed, during AMJ across almost all sectors of permanent and marginal sea ice (Beaufort, Chuckchi, East Siberian, Laptev, Kara Seas) and over the Baffin Bay. In the last two
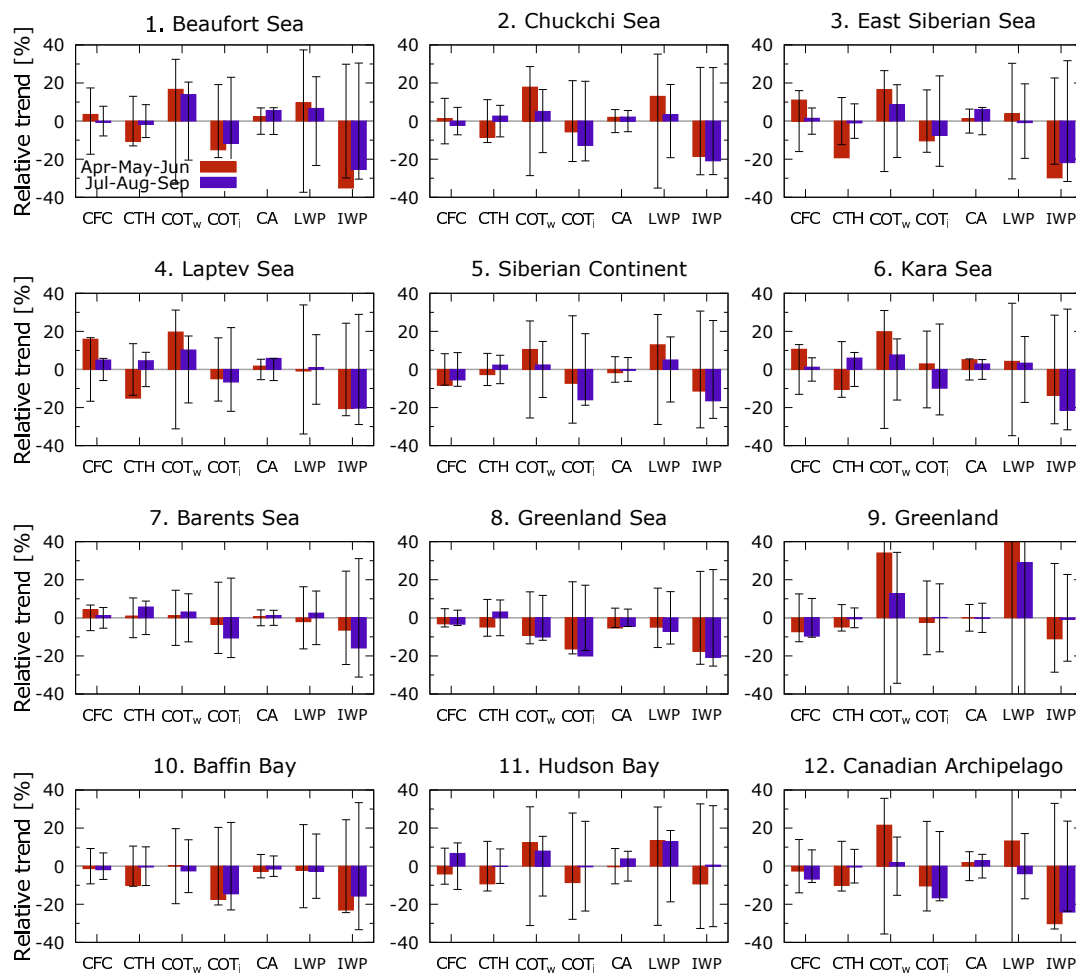
Figure 8. Trends (and 2-σ standard deviation) of cloud properties for the twelve sectors defined in Fig. B1 for spring (April - May - June, red bars) and summer (July - August - September, purple) months. The y-axis display the change relative to the leading season in 1996 and express the total change throughout the full record throughout 2016.

decades CTH in these regions has decreased by 10% on average. In JAS, however, CTH increases significantly from the Fram strait, throughout the Barents and Laptev Seas, closer to the Pole, and western Siberia, with a less pronounced positive trend for Greenland (+4%) and a more pronounced one for the Hudson Bay (+8%), albeit non significant. Total COT is split into liquid and solid cloud phases. The geographic distribution of the trends in Fig. 7 provides insight into which areas are responsible for the positive pan-Arctic trend in τ of liquid clouds (τ-water) and for the negative trend for ice clouds (τ-ice). τ-water increases across the whole Arctic in AMJ except over the Atlantic sector and the southern part of the Hudson Bay. The positive trend is maintained over north Greenland, Canadian Archipelago, North Pole and part of the Eurasian continent also during JAS. A positive trend of τ-water is correlated with a trend of opposite sign for τ-ice: this holds for all regions of permanent and

255 marginal sea ice, for the Canadian Archipelago and for the Hudson Bay. Conversely, Greenland, Baffin Bay and the Atlantic sector show a different behavior: there is a 34% increase in τ-water during AMJ and 22% increase in JAS. Notwithstanding the increase over localized areas (e.g. north Greenland), mean τ-ice over the Arctic regions remains nearly unchanged in both seasons. The liquid phase of clouds does not increase across the Fram Strait, whereas the ice phase decreases by roughly 20% in both AMJ and JAS periods. Finally, the Atlantic sector (the Greenland and the Norwegian Seas) show decreases in the COT

260 for both the liquid and solid cloud phase during AMJ and JAS.

    The rightmost polar plots of Fig. 7 show seasonal trends in cloud albedo (CA), for which a marked change of the spatial rather than temporal scale is observed. To a certain extent, the CA trends are geographically correlated with those of CFC and τ-water. Individual regions are grouped in a similar manner to the R^{TOA} polar plots: comparable distribution of CA are found over the most eastern and most western Arctic Seas (Beaufort and Chuckchi, East Siberian, Laptev, and Kara Seas). Positive trends are

265 almost invariably distributed over water masses, the Canadian Archipelago and the northern part of Greenland, irrespective of the season. In contrast, clouds become darker at lower latitudes, southern Greenland and the Atlantic sector. Over the Siberian land masses this is not observed, and CA changes in the region, besides being small, are attributed to a competition between changes in CFC and τ-water. The loss of albedo due to cloud dissipation is compensated by the increment in albedo through increased τ-water.

270   To facilitate a quantitative seasonal comparison between the Arctic sectors, Fig. 8 shows the trends and the standard error (i.e. 2-σ standard deviation, see App. 2.2) of five cloud properties (CFC, CTH, τ of water and ice phase, CA) together with trend of liquid (LWP) and ice water path (IWP), from the same cloud record (Stengel et al., 2020). Changes in R_{λ}^{TOA} depend in the first place on changes in cloudiness and τ (irrespective of the phase), which in turn is a function of LWP, droplet/crystal effective radius (r_{eff}) and air density ρ (i.e. $\tau = 3/2 \times \text{LWP}/\rho\, r_{\text{eff}}$). The sign of LWP and IWP trends confirm the τ trends. We

275 infer that τ-water has increased as a result of the positive change of LWP and/or a concurrent systematic pan-Arctic decreasing trend of r_{eff} (see Fig. C1).

3.2 Cloud radiative forcing

We compute the net radiative forcing, $\bar{F}^{cld}$ or CRF, due only to clouds. The flux data are taken from the cloud record (Stengel et al., 2020) (see App. 2.2). The difference between F^- and F^+ is the net radiation $\bar{F}$ and CRF $= \bar{F}^{all} - \bar{F}^{clr}$. The multi-year

280 mean and trends of SW, LW and total CRF at the surface are plotted in Fig. 9.

    At pan-Arctic scale clouds exert a negative SW radiative forcing of -58.7 and -63.8 W m^{-2} in AMJ and JAS, respectively. In the same seasons, the LW component amounts to $+46.9$ and $+46.1$ W m^{-2}, and the multi-year mean of total CRF is -11.8 and -17.6 W m^{-2}. However, CRF is seasonally and regionally partitioned: clouds' total radiative forcing at the surface is positive over bright areas as a result of LW offsetting SW. For instance, total CRF over Greenland is $+14.9$ and $+23.5$ W m^{-2},

285 which corresponds to the Arctic sectors over which clouds reflect the least in absolute SW (-19.8 in AMJ and -21.3 W m^{-2} in JAS) and emit 36.2 in AMJ and 43.3 W m^{-2} LW radiation in JAS. The minimum total CRF is measured over the Baffin Bay, the Atlantic corridor and Barents Sea in AMJ (-51.1 W m^{-2}) and JAS (-43.4 W m^{-2}). This is explained by the combined effect of the brighter surface, increasing SW reflectivity and damping upwelling LW, and comparatively low optical COT
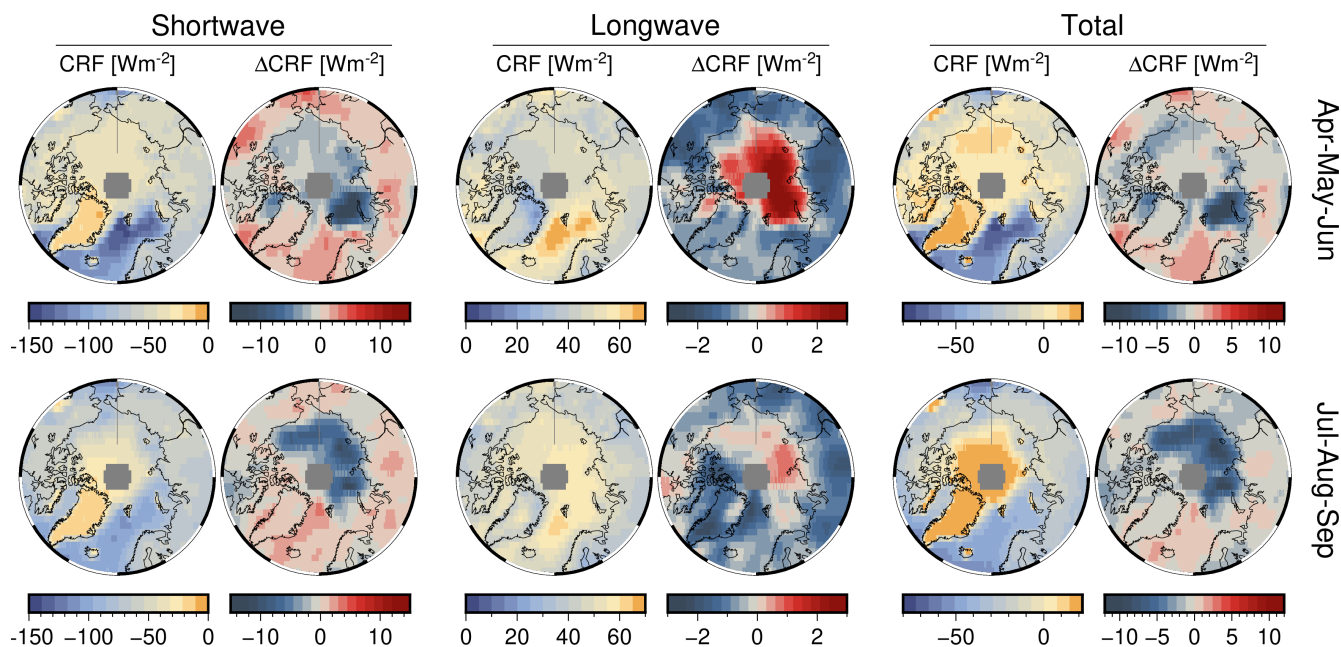
Figure 9. For Arctic spring (AMJ, top) and summer (JAS, bottom), the multiyear mean Cloud Radiative Forcing (CRF) and total change ΔCRF at the surface.

(irrespective of the phase) over Greenland (8.4±7.3 in AMJ and 6.7±3.5 in JAS). For the same seasons, darker surfaces of
290 the Atlantic corridor and Baffin Bay emit LW more effectively. However, SW offsets LW and total CRF turns negative owing
to larger τ-water over the Greenland Sea (14.5±3.4 in AMJ and 15.6±3.3 in JAS) or the Baffin Bay (14.6±5.3 in AMJ and
13.4±3.0 in JAS).

The climatological annual pan-Arctic total CRF (Fig. D1) is positive at BOA (+9.2 W m^{-2}) with the sole exception of the
Greenland Sea (−4.2 W m^{-2}). Minimum values are found over Baffin Bay (+3.3 W m^{-2}) and the Barents Sea (+5.4 W m^{-2}).
295 Over Arctic ocean, total CRF amounts to +7.0 W m^{-2}, which is lower than the +10 W m^{-2} reported by Kay and L'Ecuyer
(2013), while over land masses clouds warm the surface by +11.0 W m^{-2}. Consequently, the Arctic surface is warmed by
clouds throughout and our results are qualitatively consistent with the current knowledge (Zygmuntowska et al., 2012; Kay
and L'Ecuyer, 2013; Intrieri et al., 2002). The maximum cloud warming at BOA occurs over Greenland (AMJ +14.9 W m^{-2},
JAS +23.5 W m^{-2}) and to a lesser extent above sea ice covered regions in AMJ (East Siberian Sea +6.9 W m^{-2}, Beaufort
300 Sea +5.7 W m^{-2}, Laptev Sea +2.1 W m^{-2}) and JAS (East Siberian Sea +0.4 W m^{-2}, Beaufort Sea +6.5 W m^{-2}). Otherwise,
the other Arctic regions show a negative total CRF, from −51.1 W m^{-2} over Greenland Sea and −42.2 W m^{-2} Barents Sea
in AMJ to the −39.2 W m^{-2} over those regions influenced by the climate of low latitudes (Baffin Bay, Greenland and Barents
Seas) and −30.7 W m^{-2} and −22.4 W m^{-2} over the Hudson Bay and Kara Sea in JAS, respectively.

From the CRF trends of the last two decades (Fig. 9), clouds over the perennial sea ice zone are increasingly cooling TOA

305   (see Fig. D1) and BOA alike, while being neutral to positive over the Atlantic corridor and land masses at low latitudes. In AMJ

months, maximal cooling trends at TOA (BOA) are for Kara and Laptev, up to $-2.7\,(-2.4)\,\mathrm{W\,m^{-2}\,decade^{-1}}$, and extend along

the Polar Circle up to the northern section of the Baffin Bay through the Chuckchi Sea, albeit dropping in magnitude to -0.9

$(-0.8)\,\mathrm{W\,m^{-2}\,decade^{-1}}$. During AMJ, clouds have increasingly cooled the Siberian land masses and the marginal sea ice

zones at an average rate of $-0.4\,\mathrm{W\,m^{-2}\,decade^{-1}}$, with the Barents Sea undergoing the strongest CRF drop by $-2.5\,\mathrm{W\,m^{-2}}$

310   $\mathrm{decade^{-1}}$. Otherwise, CRF trend at TOA and BOA during JAS varies from slightly positive over land masses, such as Eurasia,

$+0.1\,(+0.1)\,\mathrm{W\,m^{-2}\,decade^{-1}}$, over open waters in the Atlantic sector, the southernmost portion of Baffin Bay, and the Bering

Strait. Cooling trends due to clouds are identified over Greenland for both seasons having a rate of $-0.5\,\mathrm{W\,m^{-2}\,decade^{-1}}$.

4   Discussion and conclusions

In the last two decades, the set of analyzed parameters provides a coherent geophysical picture: the Arctic R_λ^{TOA} has declined.

315   However, this decline is less than that expected as a result of the loss of sea ice. We attribute the reason for this decreasing

trend to be a decrease in sea ice, compensated for by wetter Arctic clouds. This results from their increasing water content

and a concurrent simultaneous decreasing ice content. Atmospheric moisture fluxes are increasing as a result of more open

waters and transport (Boisvert and Stroeve, 2015; Rinke et al., 2019). Marked regionality and seasonality of R_λ^{TOA}, cloud

properties and CRF across the Arctic is identified in four macro-regions, consistently exhibting similar behavior: Greenland,

320   the permanent and marginal sea ice areas, the Atlantic sector, and the land masses al lower latitudes.

To some extent, Wang and Key (2005b) anticipate the results of our work. The downward trend in broadband albedo of

$-1.40\%\,\mathrm{decade^{-1}}$ between $1985-1999$ is confirmed by our negative all-sky R_λ^{TOA} trends, implying a sustained sea ice loss

after 2000 and general darkening of the Arctic surface. However, the regional patterns match neither our results nor most recent

knowledge (Hofer et al., 2017). The annual increase of 0.6% in CFC over Canadian Archipelago, Chuckchi Sea and Siberia

325   and, in JAS, over Greenland reported in Wang and Key (2005b) is probably explained by the limited length of the analysed

record. Trends in CFC over Greenland, for instance, level out before 1995 but turn strongly negative afterward, contributing

to a significant loss of the ice shield mass (Hofer et al., 2017). This explains the nonexistent clouds' τ trend in Wang and Key

(2005b), which is in contrast to the significant moistening across most of the Arctic of Figs. 6, 7 and 8.

Greenland has a unique behavior: R_λ^{TOA} trends at all wavelengths are positive, irrespective of the season (Fig. 6). The AMJ

330   R_λ^{TOA} trends, up to 5%, are even larger than those for JAS. This result is particularly surprising, given the insignificant CFC

trend (Fig. 7,8), thus not contributing to an increase of the overall reflectance. Similar behavior is found in the Hudson Bay and

Canadian Archipelago, which show an increase in reflectance, in contrast to a general darkening of the Arctic. The mechanism

by which these regions increase R_λ^{TOA} lies in the link between LWP and CA, through τ-water. In fact, τ-water changes sustain

the correlated R_λ^{TOA} changes because of the non-linear relationship of CA to τ-water via LWP. It follows that a R_λ^{TOA} loss

335   is overcompensated by wetter clouds in the northern sector and by increased snowfall in the southern part of the Greenland

continent. Cloud LWP has increased by 28-30% over Greenland and by 14-16% over the Hudson Bay and the Canadian

Archipelago, having positive τ-water trends of 30%, 14% and 22%, respectively. Notably, the seasonal behavior of τ-water, increasing over Greenland, is not associated with CFC loss and a positive CRF change in the last 20 years. In contrast, cloud dissipation, increased by anticyclonic activity and concurrent temperature inversion strengths, is responsible for enhanced

340 insolation at the ground and melting (Hofer et al., 2017). JAS R_{560}^{TOA} changes over the Hudson Bay are exceptional. They are correlated with a 9% increase in τ-water and minimal CRF changes. This area shows one of the largest CFC increases during JAS months (Fig. 8), also corroborated by similar significant changes in AMJ and JAS observed in the reanalysis data (Fazel-Rastgar, 2020). The total CRF is -30.7 W m^{-2} while $+2.7$ W m^{-2} during AMJ. CRF trends point to a cloud cooling of the Hudson Bay at a rate of -2.9 (AMJ) and -1.3 (JAS) W m^{-2} over the last two decades.

345 Cloud forcing at the surface depends on cloud property changes. The behavior is summarized in the seasonal and regional charts of Fig. 10, in which mean value and trend of SW, LW and total CRF are shown as function of τ-water of clouds, LWP and CFC changes. It is evident that the strong relationships in AMJ and JAS between total CRF, COT, and LWP are more important in modulating radiation than CFC. While SW CRF cooling dominates over LW CRF warming, CFC changes modulate mainly the LW portion of cloud radiation in both seasons. Arctic regionality emerges from the clustering of the regions, especially in

350 AMJ and to a lesser extent in JAS. In the last two decades the net energy radiating at the surface due to clouds is decreasing. Clouds cool the surface when the upwelling SW energy dominates the downwelling LW radiation. This is the case when clouds become optically denser and hence more reflective.

Those regions characterised by a darkening surface undergo an increase in SW reflection, leading to an increasing cooling by clouds (ΔCRF<0). This takes place over the periennal sea ice zone (Beaufort, Laptev and East Siberian Seas), where a CRF

355 decrease at a rate of -1-2 W m^{-2} is associated with greater cloudiness in AMJ and increasing τ-water in JAS. Quantitatively, with values of ΔCRF$_{\mathrm{Total}} = -1.4$ W m^{-2} and ΔCF $= 3.03$ %, we obtain the total long-term sensitivity ΔCRF$_{\mathrm{Total}}/\Delta$CF $= -0.48$ W m^{-2} %$^{-1}$ over the Beaufort Sea in AMJ. The sensitivities of the SW and LW parts of CRF amount to -0.56 and $+0.84$ W m^{-2} %$^{-1}$. Although averaged over one multi-year season only, our estimation is in line with measurements reported at the same location during the SHEBA campaign (Shupe and Intrieri, 2004). The SHEBA sensitivity of ∂CRF$_{\mathrm{LW}}/\partial$CF $= 0.65$

360 W m^{-2} %$^{-1}$ was seen to offset the SW for most of the year (with ∂CRF$_{\mathrm{SW}}/\partial$CF $\in [0,1]$ W m^{-2} %$^{-1}$), thereby warming the surface while cloud cooling took place only in midsummer months. Accordingly, we report a net total (SW+LW) sensitivity of -0.13 W m^{-2} %$^{-1}$ in JAS, meaning that the SW cooling takes over LW warming during the Arctic JAS in the record. The greenhouse effect from increased CFC in AMJ over these regions is not directly linked to the retreat of sea ice, the onset of which is in late May (Smith et al., 2020). Rather it is attributed to the enhanced convergence of atmospheric water content originating from open Arctic oceans during years with anomalously low sea ice extent (Kapsch et al., 2013). Our results imply

365 that this mechanism is not only evident in the year-to-year variability of exceptional sea ice lows, but is also a long-term component at decadal time scales, during which atmosphere-ocean coupling effects are predominant.

With the sole exception of the East Siberian Sea in JAS where τ-water of clouds grows in spite of a lower content of liquid water (Δr$_{\mathrm{eff}} \approx +0.3$%, see Fig. C1), any positive τ-water trend corresponds to LWP changes for both seasons. Although not

370 surprising, we note that the AMJ changes in CRF do not correlate with either LWP or COT. In the JAS months, however, larger cloud optical densities and LWPs are matched by a decrease in CRF at the surface. This is the combined outcome of
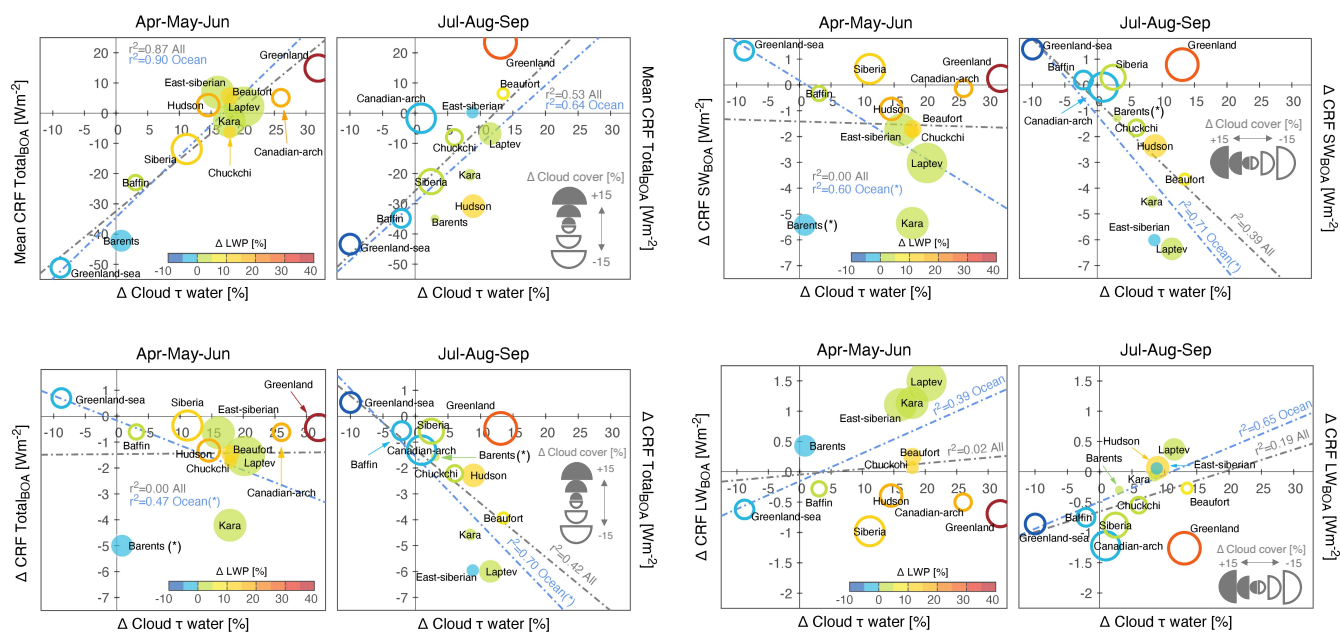
Figure 10. Regional and seasonal mean CRF (top left panel), SW CRF (top right), LW CRF (bottom right) and total CRF (bottom left) trends as function of τ trends for liquid clouds. The concurrent change in LWP is color coded while the increase (decrease) in cloudiness is given by a filled (outlined) circle.

two effects: more insolation in the JAS months results in a more efficient SW scattering by cloud droplets and the darkening of the surface lowers the LWP threshold necessary for the CRF_{SW} to dominate CRF_{LW}. Excluding Barents Sea, the variance of ΔCRF during AMJ is narrower (-4.2 to $+0.9\,\mathrm{W\,m^{-2}}$) than during JAS (-6 to $+0.4\,\mathrm{W\,m^{-2}}$). This is evidence for the
375 importance of radiance from the underlying surface, which is larger in AMJ than in JAS.

In addition to loss of clouds, the extended ice melt in Greenland is also known to be reinforced by low altitude liquid water clouds having sufficient opacity to allow the enhancement of downwelling LW flux but also being optically thin enough to allow a significant fraction of the SW flux to pass. This results in the surface being warmed (Bennartz et al., 2013). Such clouds occur within the range of LWP between $10\,\mathrm{g\,m^{-2}}$ and $60\,\mathrm{g\,m^{-2}}$ corresponding to the range of enhanced CRF at BOA.
380 Fig. 8 shows that the increase of cloud τ-water and LWP over Greenland is among the largest throughout the whole Arctic for both seasons. We attribute a reduction in melting to the increased wetting of clouds (ΔLWP $\geqslant 40\%$ at current typical LWP values). Similarly, during AMJ, Greenland and the Canadian Archipelago exhibit a rather small ΔCRF along with a large increase in τ-water and R_{560}^{TOA}. Enhanced surface cooling by clouds is thus less efficient. These regions are predominantly land or land/water mixtures, accordingly modulating the SW-to-LW flux balance.
385 Advances in observational techniques and process-level research are needed to assess unambiguously the relative roles of temperature T and atmospheric particulate matter in determining cloud thermodynamic changes. In the absence of a systematic, pan-Arctic, aerosol indirect effect due to decreasing trends of ice or cloud condensation nuclei (IN/CCN), higher condensation

rates (i.e. positive LWP trends) of small-sized cloud droplets can only nucleate and grow by a combination of changes in Arctic boundary layer depth within a saturated air volume. Different temperature regimes influence CA changing the $\tau - \mathrm{r_{eff}} - \mathrm{LWP}$
390 relationship (Tselioudis et al., 1992) and favour droplet growth over condensation rates and vice versa (Lohmann et al., 2000). To this end, the driver of, mostly decreasing, $\mathrm{r_{eff}}$ trends (see bottom plot of Fig. C1) remains unclear. $\mathrm{r_{eff}}$ size spectrum is modulated by the amount of water vapor and available particulate. While model and satellite data show a general moistening of the Arctic (Rinke et al., 2019; Boisvert and Stroeve, 2015), local on-ground (Graßl and Ritter, 2019) and pan-Arctic satellite (Linlu et al., 2021) evidence of a decrease in total aerosol burden is growing. However, IN/CCN can not be directly inferred
395 from changes of column-integrated extinction of total aerosol load. Assuming a CCN decrease is in contradiction with the $\mathrm{r_{eff}}$ reduction via the Twomey effect. Alternatively, we speculate that the change in size spectrum or aerosol type might lead to optimal IN/CCN size and hygroscopicity, although the total aerosol amount has decreased. Satellite-derived single $\mathrm{r_{eff}}$ values are only representative of the droplet/crystal population at a level of ≈ 1-τ from the cloud top (Platnick, 2000). We recommend that the available and relevant spectral observations are exploited (Kokhanovsky and Rozanov, 2012; King and Vaughan, 2012)
400 to generate a pan-Arctic picture of in-cloud $\mathrm{r_{eff}}(z)$ profiles, which would optimally complement surveys based on spaceborne active techniques (Chan and Comiso, 2013; Matus and L'Ecuyer, 2017). $\mathrm{r_{eff}}(z)$ profiles, together with aerosol speciation at high latitudes (Schmale et al., 2021) and cloud bases (Lelli and Vountas, 2018), are essential in two ways. First, they constrain IN/CCN activation, supersaturation and, therefore, cloud particle number concentrations (Zheng et al., 2015; Grosvenor et al., 2018). Second, cloud fields will be more accurately separated according to their phase (liquid, ice and mixed-phase) and
405 layering (low, mid, high-level and multi-layered). We consider our results as upper bounds and more vertical resolution will improve our understanding of the evolution of clouds in the Arctic.

From a modelling standpoint, we can validate past results (Morrison et al., 2019), for which the increase in cloud τ-water and LWP are projected to extend well beyond the middle of the present century. Constraining the cloud microphysics and thermodynamic phase will not only be crucial to project future Greenland melting (Hofer et al., 2019) but also to assess the
410 sign and strengths of total cloud feedbacks (Gettelman and Sherwood, 2016). Given the actual and future Arctic temperatures, ice will be increasingly depleted. Hence, τ-water and LWP will increasingly determine net cloud feedbacks (Bjordal et al., 2020). When the cloud ice phase turns to water a negative feedback is expected due to the offsetting of LW by SW. If climate models do not correctly capture this, i.e they do not incorporate more supercooled liquid than mixed-phase clouds (Lohmann, 2002), unrealistically large amounts of ice result, effectively reversing the sign of the net cloud feedback. We consider that this
415 is one reason, which may explain in part the discrepancy between the atmospheric components (CAM) of the Community Earth System Model 2 (Gettelman et al., 2019, Fig. 2). We note that a CAM5 positive cloud feedback at Arctic latitudes becomes negative in CAM6 as a result of an improved modeling of the cloud phase. Coherently, CAM6 projects a warmer Arctic with increased rainfall rates in JAS at the expenses of snow precipitation (McCrystall et al., 2021), as the outcome of poleward moisture streams and wetter Arctic clouds.

420 In summary, we have identified expected decreasing and unexpected increasing trends of R_λ^{TOA} during the period 1996 to 2018 in the Arctic. We then investigated the possible origins of the unexpected increases of R_λ^{TOA}, analyzing cloud optical and physical parameters. We conclude that clouds, through changes in their optical properties explain the increase in R_λ^{TOA} and

that implies an increasing amount of supercooled liquid cloud droplets. The higher reflectance of clouds results in a more negative radiative forcing at the surface, thereby locally dampening Arctic Amplification. However, cooling by clouds implies

425   the strengthening of the meridional temperature gradient. We expect this will lead to increase the inflow of warmer and moister air masses from the lower latitudes into the Arctic climate. This may then either further decrease Arctic Amplification by generating more supercooled liquid water cloud, or possibly enhance Arctic Amplification by the increase input of warmer air, or some combination of the two. Future model projections of the Arctic climate must take into account these effects to accurately predict the impact of anthropogenic emissions of greenhouse gases and short-lived climate pollutants.

Appendix A: Detailed description of reflectance data harmonization

430

Table A2 shows that overpass time, swath and footprint size differ among the sensors used in this work. These sensors are payloads on satellites which fly in sun synchronous orbits having different equator crossing times. Errors in the R_λ^{TOA} in the Arctic arising from the 30-minutes time lag are considered negligible for averaged R_λ^{TOA}. Monthly aggregation leads to higher means for finer spatially-resolved instruments than otherwise. Thus, intra-sensor radiometric R_λ^{TOA} harmonization is a prerequisite

435 for the creation of calibrated time series and the detection of trends. Different application-dependent approaches have been already employed. Krijger et al. (2007) derives gain correction factors based on the number of cloud-free scenes as function of spatial resolution for maximization of usable trace-gas retrievals. Tilstra et al. (2012) separates the influence of scattering geometry and cloud occurrence to correct SCIAMACHY reflectances for the computation of the aerosol absorbing index at UV wavelengths. Both approaches are not suited for our goal. The former aims at the removal of the influence of clouds, which

440 are a primary component of the Arctic environment. The latter examines instrumental performance in a spectral region that is not of direct interest as a result of potential radiometric degradation of sensors and of higher sensitivity to aerosols, whose radiative effects are comparatively small in the troposphere. Conversely, Hilboll et al. (2013) elaborate a method to explicitly take into account the difference in the ground pixel size and spatial misalignment across sensors. This is achieved by projecting the orbit of one instrument onto that of a second instrument. In our case, we select SCIAMACHY as reference sensor due to

445 its well-calibrated spectral behaviour and because it overlaps with both GOME and GOME-2A. A conservative area-weighted remapping scheme Jones (1999) is employed to derive the factor matrix transforming GOME-2A reflectances as they were measured by SCIAMACHY. Due to the frequent overlaps at high latitudes, only those GOME-2A orbits closest in time to SCIAMACHY are remapped. To extend the time series beyond the loss of Envisat in April 8th, 2012, full SCIAMACHY geolocations, comprising 431 orbits per month, have been used as target tessellation for the rest of the GOME-2A record. The

450 downside of mimicking SCIAMACHY orbits, due to its design of alternating nadir and limb swath states, is the reduction of the GOME-2A sampling rate. This is compensated for in part by the inherently different cross-swath viewing geometries and changes in illumination. GOME projection onto SCIAMACHY has not been implemented. Not only the two sensors overlap for a limited period of six months, but the relatively low sampling rate of GOME would have resulted in suboptimal statistics, even at a monthly scale. Validation has shown that GOME R_λ^{TOA} are consistent with those of SCIAMACHY (see Fig. 3 in main

455 text). Remaining intra-sensor inconsistencies that cannot be compensated for, such as changes due to the dynamic radiometric response over dark-to-bright surfaces, will be eventually accounted for by the trend model.

We tested the assumption that bidirectional surface effects do not introduce error in the detection of the temporal trends of R_λ^{TOA} by inspecting monthly distributions of the scattering angle throughout the record, separately for each sensor. This is needed because R_λ^{TOA} is, by definition, a directional quantity and depends on the scattering geometry. It has been found

460 that the monthly data aggregation of all individual line-of-sights almost fully cover the hemispheric solid angle, incorporating the hot spots of different scene types. The mean value of the scattering angle of $98.48°$ in 1996 shifts to $98.41°$ in 2018 for AMJ (-0.08%) and from $97.03°$ to $96.55°$ for JAS (-0.51%). These shifts are considered uncritical for this study and do not introduce artefacts in the record.

Appendix B: Trend and significance estimation

Trend detection is performed with the same technique for all the variables and parameters in this study. We illustrate the steps with reflectances. Dropping the subscript λ for readability, the R_λ^{TOA}, measured by sensor i and aggregated at month t, $Y(t,i)$, are modelled with

$$Y(t,i) = \mu_i C(t,i) + S(t,i) + \omega_i t + \delta U(t,i) + N(t,i). \tag{B1}$$

The $\mu_i C(t,i)$ are the intercept of the regression line, $S(t,i)$ is the seasonal component of the time series, ω_i the desired trend value and $N(t,i)$ the noise residuals embedded in the model after the regression is carried out. The term $\delta U(t,i)$ stands for the product of the level shift δ among the respective sensor records (Hilboll et al., 2013) with the step function $U(t,i)$ needed to concatenate the individual time series at time $T_i(t=0)$ (Lelli et al., 2014). The seasonality $S(t,i)$ is accounted for by subtracting the average R_λ^{TOA} of each month from the respective monthly value. This method is similar to the harmonic expansion in Fourier series, in which the coefficients are derived in a least squares sense. Both methods are equivalent and the choice of one method rather than the other does not introduce significant errors (Mieruch, 2009). The term $\delta U(t,i)$ is embedded by calculating the seasonality separately for each instrument. Its function is to correct possible artefacts due to the different overpass times of the respective spaceborne platforms. While the offsets $\mu_i C(t)$, centred about their mean absolute value at the beginning of the time series, tend to zero upon the anomaly calculation, the last unexplored portion of the data is the noise component $N(t,i)$, in which autocorrelative effects are buried. The R_λ^{TOA} time series are persistent in time and the autocorrelation $\rho \nrightarrow 0$ for all Arctic regions after one lag. Thus, not all noise components of the record are random and cannot be treated as gaussian. This limits the informative value of any significance test and hinder the detection of trends. Block bootstrap resampling (Efron and Tibshirani, 1993), belonging to the group of nonparametric methods, does not require prior knowledge of the analytical form of the underlying statistics of potentially non-normal data (Mudelsee, 2010). They rest on the block length of the effective independent random sample (Wilks, 1997, Eq. 19). An empirical sample distribution of the trend magnitude ω is then computed scrambling n times the blocks of the original record. The resulting empirical distribution approximates the unknown ω probability density function. This allows to find the 2-σ_ω interval needed for a confidence level at 95%. For all locations where the ratio $|\omega/\sigma_\omega| > 2$, the trend magnitude ω exceeds natural variability and is termed statistically significant.

Appendix C: Uncertainty propagation in the cloud record and sensitivity

The cloud data set is generated using an optimal estimation framework, which allows propagation of random and systematic uncertainties into the pixel-based retrievals. Following Eqs. 2–5 in Stengel et al. (2017), for each location i at time t, we calculate the true variability $\sigma_{\mathrm{true}}(i,t)$ and the uncertainty of the mean $\sigma_{\langle x \rangle}(i,t)$ for the cloud property x from the mean of the squared pixel-based uncertainties $\langle \sigma^2(i,t) \rangle$ and its standard deviation $\sigma_{\mathrm{SD}}(i,t)$. Further, aggregation into monthly averages requires the uncertainty correlation c, or heterogeneity, relating $\sigma_{\mathrm{SD}}(i,t)$ to $\sigma_{\mathrm{true}}(i,t)$. Because c is not known beforehand, setting it to a fixed value is an arbitrary choice that does not account for the spatial and temporal relationship of algorithmic

errors at pixel level throughout wide-scale cloud fields. Hence, we exploit the fact that $\sigma_{\mathrm{SD}} \to \sigma_{\mathrm{true}}$ when $c \to 1$. This holds when the spatial sampling is the highest, thus we scale the number of successful retrievals of the cloud property x to $c \in (0,1]$ and compute the c-dependent $\sigma_{\mathrm{true}}(i,t)$ and $\sigma_{\langle x \rangle}(i,t)$. Temporally, both σ_{true} and $\sigma_{\langle x \rangle}$ change as function of c. Seasonal trends of c reveal an overall increase of maximum 3% in AMJ and 1.9% in JAS over the Barents throughout the East Siberian

500 Sea, whereas c over Greenland, Hudson Bay and the Canadian Archipelago exhibits a decrease of 0.6% in both seasons. This translates into a change of $\pm 0.5\%$ and $\pm 0.4\%$ in σ_{true} and $\sigma_{\langle x \rangle}$, respectively. With this approach, the clouds' heterogeneity of the monthly averages is related to retrieval errors predominantly in the spatial but not in the temporal dimension. Limited to an observational analysis of the cloud record, while uncritical for trend assessments only, $\sigma_{\langle x \rangle}$ can be then successively used to label as meaningful those sensitivities of CRF to susceptible cloud property x, whose trend exceeds $\sigma_{\langle x \rangle}$.

505 **Appendix D: Additional description of ozone trends**

R^{TOA} trends at 560 and 620 nm capture the Chappuis ozone absorption band having a broadband maximum centred about 602 nm and two wings stretching between 525 and 675 nm (Gorshelev et al., 2014). Analysing seasonal stratospheric and total column ozone, we are able to determine an effective modulation of R^{TOA} trends by ozone. Ozone data in Fig. A1 are locally derived from GOME, SCIAMACHY and GOME-2A (Coldewey-Egbers et al., 2005) for the total column values (Coldewey-

510 Egbers et al., 2005) and with SCIAMACHY and the OMPS Limb Profiler measurements for the stratospheric column portion (Flittner et al., 2000; von Savigny et al., 2003; Arosio et al., 2019) in the time window 2003 – 2018. The tangent height of 41.3 km is selected due to its highest sensitivity to stratospheric ozone concentrations, which peaks about that altitude. Ozone is produced in the tropics and circulation patterns transport it poleward. It is usually located above the tropopause and its concentrations are higher during winter months and lowest in summer months. Despite its high variability through the year,

515 total ozone trends are generally small in the order of $\pm 1\%$. Focusing on the Arctic, average total ozone is 353 DU and also exhibits a distinct maximum in spring months and a minimum in summer months. The Arctic-wide trend of total ozone is positive by 3.9 DU (+1.1%) decade^{-1}, in line with global values.

  Greater significant positive trends, ranging from +4 to +10% decade^{-1}, are found in stratospheric ozone. They are centred above Greenland and stretch out along the 75°N parallel from the Greenland Sea through the Beaufort Sea in spring (AMJ)

520 with a longer tongue over the Siberian Continent in summer (JAS). Contrasting the total with the stratospheric column yields the influence of the tropospheric ozone only. For those locations where the trend in total ozone is absent but positive in the stratosphere, a negative tropospheric trend can be deduced. This mechanism is consistently found above 70°N from the Canadian Archipelago through to the East Siberian Sea, irrespective of the season, together with the sustained positive trend above the Atlantic (the Greenland Sea), the neighbouring Barents Sea and the northern part of mainland Greenland (Gaudel

525 et al., 2020). This reverses in a dipole fashion in JAS, when patterns of positive trends in total ozone are advected southward. In summary, when analysing $R_{\lambda}^{\mathrm{TOA}}$ trends at $\lambda = 620$ nm, and to a lesser extent 560 nm and 665 nm, changes in ozone contribute for those Arctic sectors affected by the meridional dynamics of air masses in which the stratospheric ozone is increasing. The
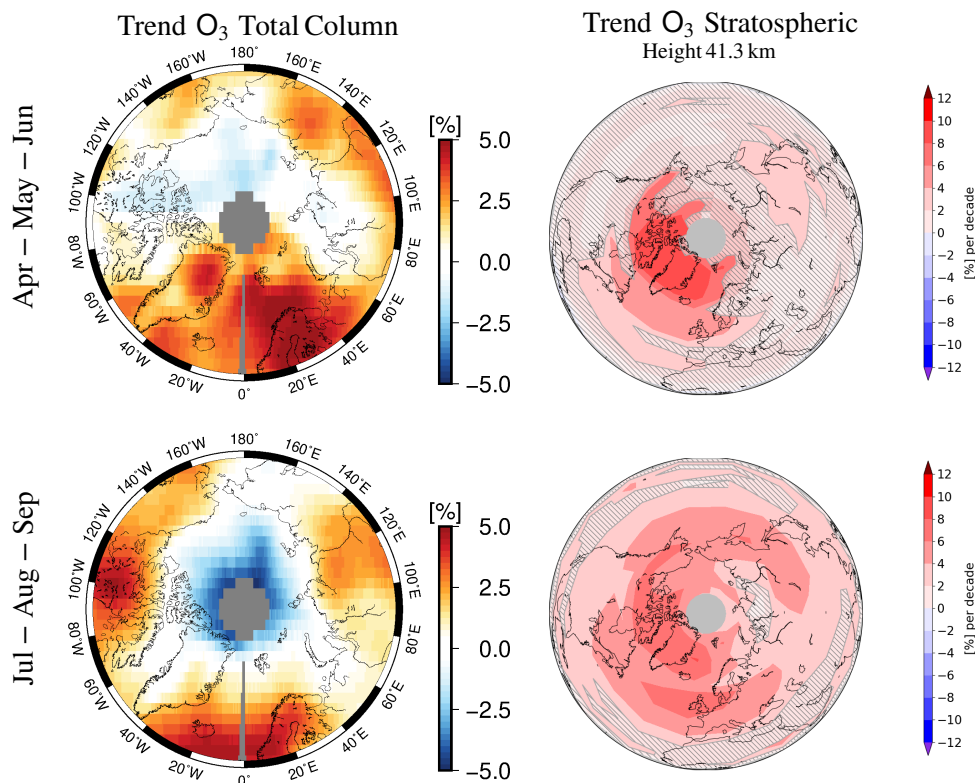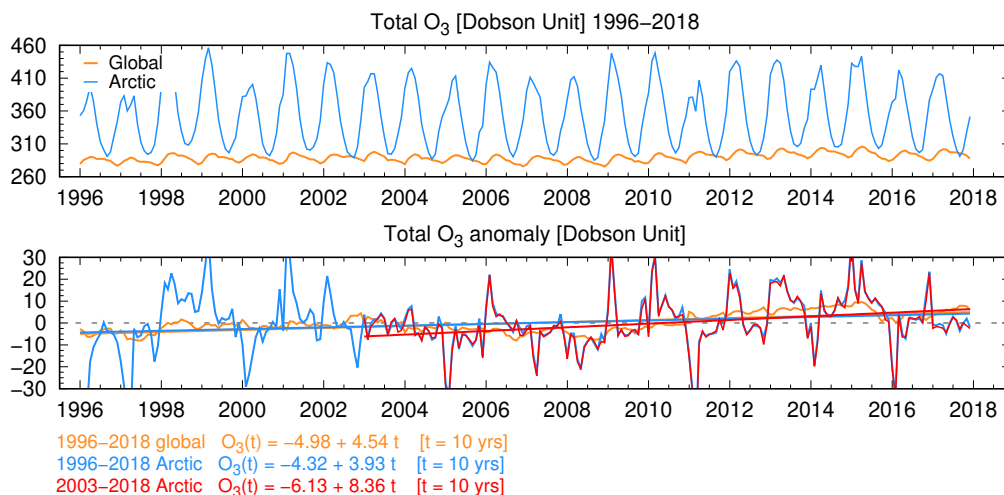
Figure A1. Top: global and Arctic record of total ozone with the respective anomalies and trends. The Arctic time series has been additionally shortened to match the length of the stratospheric ozone column. Bottom: trends (% decade^{-1}) of total (left) and stratospheric (right) ozone between 2003 and 2018 are plotted for spring (AMJ) and summer (JAS) months.

most eastern Arctic sectors (East Siberian, Laptev and Kara Seas) have a smaller contribution from ozone changes than the western sectors. This is consistent with a neutral ozone trend observed over these areas.

530   Finally, we speculate that a surface warming of the Arctic might inflate the tropopause, inducing the production of polar stratospheric clouds as a result of colder temperatures. Lower ozone would absorb less UV and visible radiation, cooling the stratosphere further and potentially accelerating further its depletion. Albeit within natural variability, Turner et al. (2009) held stratospheric ozone depletion responsible for a change in wind flows and patterns across the South Pole, stimulating anti-correlated changes in sea ice extent of the Antarctic continent. This hypothesis could also be tested for the Arctic, using the
535   results from this investigation.

Table A1. List of abbreviations used in the main text.

Acronym	Meaning
AIRS	Atmospheric Infrared Sounder
ASTER	Advanced Spaceborne Thermal Emission and Reflection Radiometer
AVHRR	Advanced Very-High-Resolution Radiometer
BRDF	Bidirectional Reflectance Distribution Function
BSRN	Baseline Surface Radiation Network
CALIPSO	Cloud-Aerosol Lidar and Infrared Pathfinder Satellite Observation
CALIOP	Cloud-Aerosol Lidar with Orthogonal Polarization
CERES	Clouds and the Earth's Radiant Energy System
DARDAR	raDAR liDAR combined cloud properties retrieval
ENVISAT	Environmental Satellite
ERBE	Earth Radiation Budget Experiment
GOME	Global Ozone Monitoring Experiment
OMI	Ozone Measuring Instrument
MERIS	MEdium Resolution Imaging Spectrometer
MetOp	Meteorological Operational satellite
MODIS	Moderate Resolution Imaging Spectroradiometer
OMPS	Ozone Mapping and Profiler Suite
POES	Polar Operational Environmental Satellite
SBUV	Solar Backscatter Ultraviolet
SCIAMACHY	Scanning Imaging Absorption Spectrometer for Atmospheric Chartography
SeaWiFS	Sea-Viewing Wide Field-of-View Sensor
SHEBA	Surface Heat Budget of the Arctic Ocean
TIROS	Television Infrared Observation Satellite
TOMS	Total Ozone Mapping Spectrometer
TOVS	TIROS Operational Vertical Sounder

Table A2. Specifications of the instruments and data set versions selected for this work.[a]Full coverage until May 2003. [b]Payload switched-off since July 2011. [c]Lost contact on April 8, 2012. [d] Nominal end of GOME-2C record. Foreseen extended lifetimes: November 2021 (GOME-2A), 2025 (GOME-2B), 2031 (GOME-2C).

	GOME	SCIAMACHY	GOME-2
Data availability	$1996 - 2011^{a,b}$	$2002 - 2012^c$	$2007 - 2023^d$
Level 1 data processors	5.0	8.01	6.0
Equator crossing (LT)	10:30 AM	10:00 AM	9:30 AM
Global coverage [days]	3	6	1.5
Spectral coverage [nm]	$237 - 794$	$240 - 2400$	$237 - 794$
Spectral resolution [nm]	0.38	0.44	0.48
Pixel size at nadir [km^2]	320×40	60×30	80×40
Swath width [km]	960	1000	1920
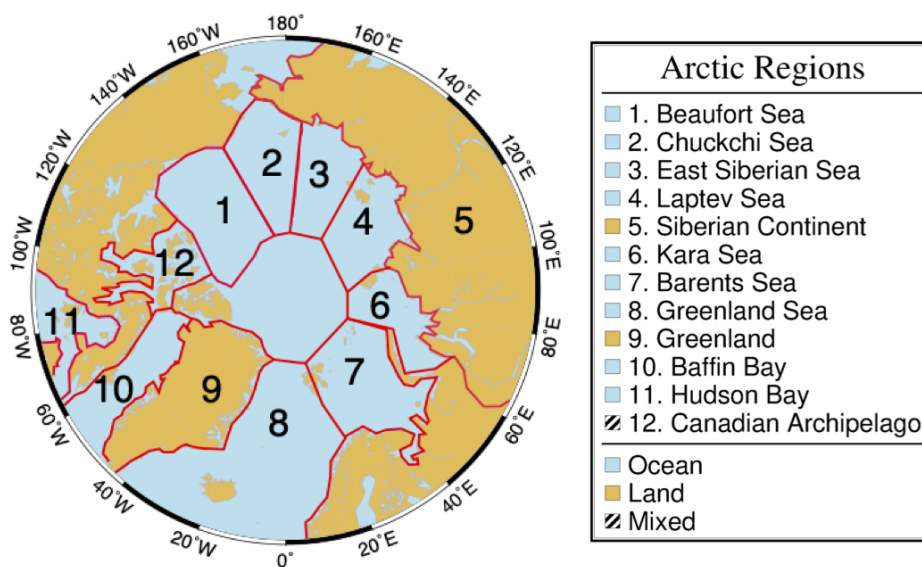
Figure B1. Definition of the Arctic climate zones, identified by distinct geophysical settings, that will be used in this study to derive local trends of R_λ^{TOA}, cloud properties and forcing. The geographical subdivision follows that of Serreze and Barry (2014) and Wang and Key (2005a).

Table B1. Multiyear seasonal means (± standard deviation) of cloud properties for the full Arctic and 12 regions of Fig. B1.

| Region | Cloud cover | | Cloud height [km] | | τ-water | | τ-ice | |
| | Cloud albedo | | r_{eff} [μm] | | LWP [g m^{-2}] | | IWP [g m^{-2}] | |
	AMJ	JAS	AMJ	JAS	AMJ	JAS	AMJ	JAS
Full Arctic	0.70 ± 0.12	0.76 ± 0.10	3.67 ± 0.57	4.14 ± 0.52	13.71 ± 5.75	14.21 ± 3.78	10.34 ± 3.86	12.05 ± 3.80
	0.52 ± 0.05	0.55 ± 0.06	11.87 ± 1.83	12.57 ± 1.43	126.21 ± 64.63	131.56 ± 41.14	148.08 ± 68.71	166.70 ± 73.02
1. Beaufort Sea	0.62 ± 0.19	0.80 ± 0.11	2.82 ± 0.62	3.33 ± 0.48	18.32 ± 8.43	12.71 ± 4.45	12.08 ± 3.67	9.90 ± 3.87
	0.60 ± 0.07	0.58 ± 0.07	10.89 ± 1.83	11.89 ± 1.62	171.35 ± 91.52	111.93 ± 50.43	179.45 ± 81.74	137.50 ± 79.72
2. Chuckchi Sea	0.68 ± 0.14	0.78 ± 0.10	3.30 ± 0.61	3.73 ± 0.50	15.69 ± 7.15	13.91 ± 4.00	10.63 ± 3.63	11.04 ± 3.80
	0.56 ± 0.06	0.58 ± 0.05	11.21 ± 1.91	11.97 ± 1.54	146.07 ± 85.95	123.31 ± 43.60	159.03 ± 73.16	151.06 ± 73.22
3. East Siberian Sea	0.68 ± 0.18	0.82 ± 0.09	2.94 ± 0.64	3.29 ± 0.48	17.43 ± 7.53	13.15 ± 4.13	11.77 ± 3.16	10.89 ± 3.85
	0.58 ± 0.06	0.58 ± 0.07	10.87 ± 1.91	11.96 ± 1.54	157.28 ± 79.00	112.23 ± 41.34	176.44 ± 65.94	153.52 ± 75.82
4. Laptev Sea	0.70 ± 0.18	0.83 ± 0.08	2.99 ± 0.61	3.34 ± 0.46	16.70 ± 7.37	14.77 ± 4.17	12.21 ± 3.34	12.07 ± 4.19
	0.59 ± 0.05	0.61 ± 0.06	10.37 ± 1.93	11.49 ± 1.54	145.73 ± 80.45	122.56 ± 41.38	179.37 ± 70.10	163.62 ± 81.67
5. Siberian Cont.	0.71 ± 0.10	0.74 ± 0.11	4.00 ± 0.55	4.47 ± 0.53	11.67 ± 5.00	15.02 ± 3.69	9.51 ± 4.28	13.02 ± 3.93
	0.47 ± 0.05	0.54 ± 0.06	12.31 ± 1.81	12.90 ± 1.34	106.21 ± 52.39	142.58 ± 40.23	136.00 ± 68.55	183.46 ± 74.40
6. Kara Sea	0.73 ± 0.16	0.82 ± 0.09	3.01 ± 0.62	3.39 ± 0.48	18.22 ± 7.77	16.69 ± 4.35	12.65 ± 3.72	12.80 ± 4.36
	0.59 ± 0.05	0.62 ± 0.05	10.08 ± 1.74	11.35 ± 1.55	151.44 ± 76.56	137.56 ± 38.87	187.25 ± 79.24	167.75 ± 79.36
7. Barents Sea	0.83 ± 0.10	0.84 ± 0.08	2.84 ± 0.47	3.38 ± 0.48	17.25 ± 4.68	17.46 ± 3.77	11.57 ± 3.65	13.31 ± 3.99
	0.59 ± 0.04	0.63 ± 0.04	10.96 ± 1.33	11.81 ± 1.67	141.73 ± 47.12	149.59 ± 36.13	152.60 ± 65.12	170.17 ± 72.77
8. Greenland Sea	0.84 ± 0.07	0.85 ± 0.06	3.18 ± 0.51	3.76 ± 0.59	14.53 ± 3.41	15.65 ± 3.30	10.81 ± 3.16	12.84 ± 3.60
	0.54 ± 0.05	0.58 ± 0.04	12.70 ± 1.31	13.23 ± 1.53	131.02 ± 34.18	147.43 ± 35.89	136.48 ± 51.25	165.13 ± 67.43
9. Greenland	0.51 ± 0.12	0.63 ± 0.11	5.32 ± 0.62	5.42 ± 0.46	8.40 ± 7.33	6.73 ± 3.47	5.97 ± 1.83	5.98 ± 1.83
	0.47 ± 0.05	0.48 ± 0.06	11.23 ± 2.42	11.30 ± 1.55	104.76 ± 134.88	73.46 ± 51.65	99.66 ± 44.58	93.83 ± 36.57
10. Baffin Bay	0.75 ± 0.12	0.78 ± 0.09	3.27 ± 0.60	3.88 ± 0.61	14.65 ± 5.29	13.36 ± 2.98	10.29 ± 3.41	11.64 ± 3.69
	0.52 ± 0.05	0.55 ± 0.05	11.55 ± 1.57	12.94 ± 1.41	129.63 ± 53.41	124.53 ± 32.97	144.34 ± 58.54	157.37 ± 68.47
11. Hudson Bay	0.73 ± 0.12	0.70 ± 0.13	3.33 ± 0.70	4.40 ± 0.64	12.93 ± 5.91	13.04 ± 3.42	9.61 ± 3.82	12.49 ± 4.52
	0.45 ± 0.06	0.51 ± 0.06	11.26 ± 1.84	13.41 ± 1.32	115.37 ± 57.56	123.51 ± 37.05	139.26 ± 62.42	176.42 ± 85.70
12. Canadian Arch.	0.65 ± 0.15	0.78 ± 0.12	3.15 ± 0.69	3.57 ± 0.55	17.24 ± 8.76	13.51 ± 4.15	11.98 ± 4.49	11.44 ± 3.97
	0.57 ± 0.07	0.57 ± 0.06	11.55 ± 1.98	12.52 ± 1.32	174.23 ± 107.76	123.08 ± 46.81	204.37 ± 105.59	162.03 ± 82.11
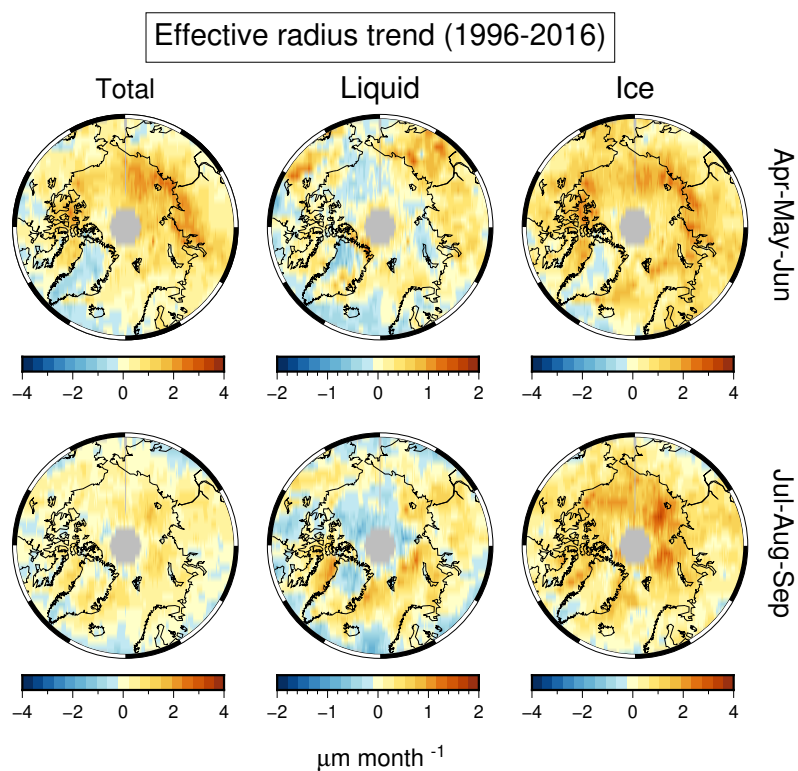
Figure C1. Seasonal trends (top: Apr-May-Jun; bottom: Jul-Aug-Sep) of cloud effective radius (in μm month^{-1}) for total cloud (left), liquid only (center) and ice only (right) thermodynamic phase. These values are representative of trends for either liquid droplets or ice crystals located at ≈ 1-τ depth from the cloud top.
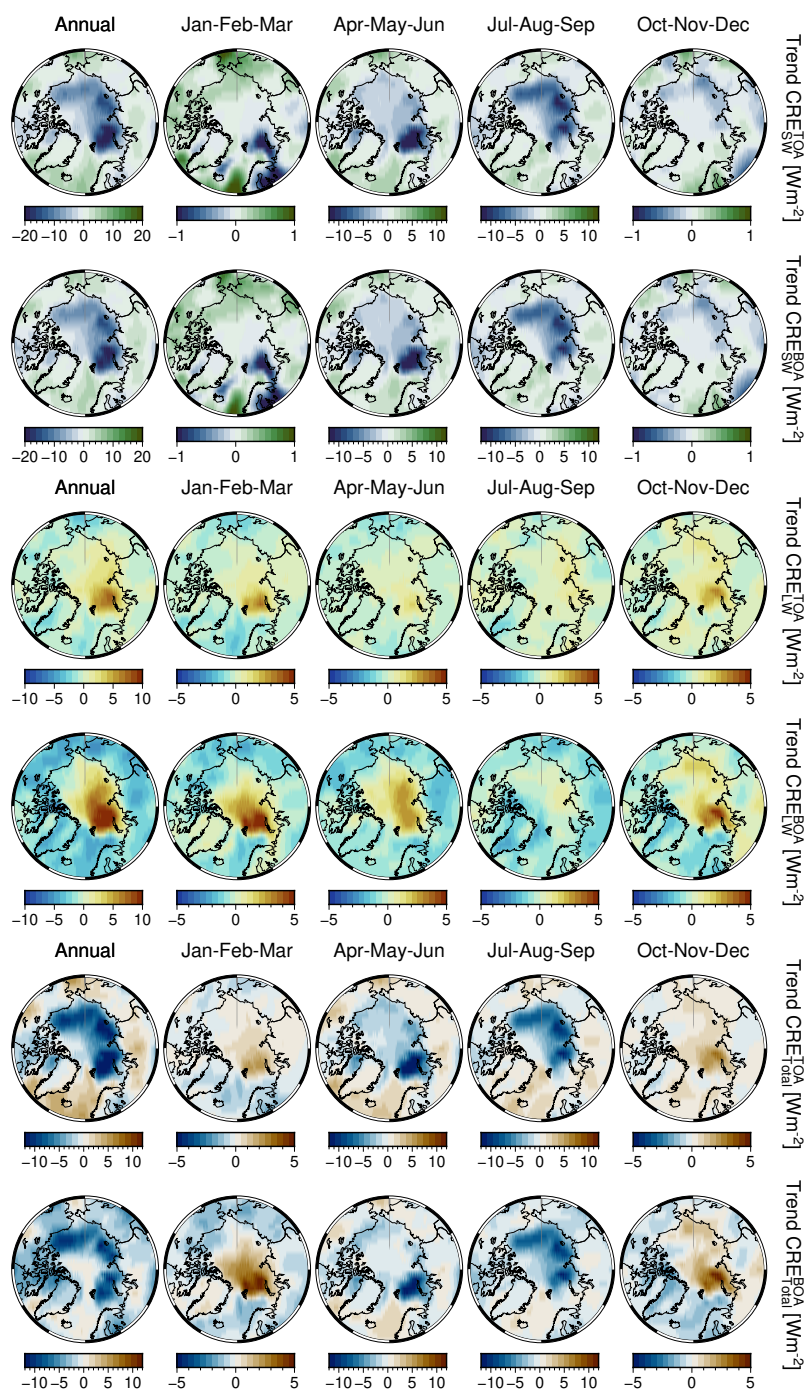
Figure D1. From left to right, annual and seasonal trends of SW (rows 1-2), LW (3-4) and total (5-6) cloud radiative effect (CRE, W m^{-2}) at TOA and BOA.

Author contributions. L.L., M.V., J-P.B conceived the research. L.L. processed orbital reflectance data, analyzed all records and wrote the manuscript. N.K., M.V. processed orbital reflectance data and analyzed the record. Funding acquisition by L.L., M.V. and J-P.B. All authors contributed to the interpretation of the results and the final drafting of the paper.

Competing interests. The authors declare that they have no competing interests.

540 *Data availability.* Spectral reflectance data are available at https://doi.pangaea.de/10.1594/PANGAEA.933905. Cloud and flux data are available at https://doi.org/10.5676/DWD/ESA_Cloud_cci/AVHRR-PM/V003.

Acknowledgements. We thank Kamesh Vinjamuri (IUP Bremen) for validation of AVHRR radiance and cloud optical properties; Carlo Arosio (IUP Bremen) for provision of stratospheric ozone data; ESA Cloud CCI working group for the processing the AVHRR data set. For valuable discussions we acknowledge Ann Fridlind (NASA/GISS), Tido Semmler, Felix Pithan (AWI Bremerhaven) and especially Kerstin
545 Ebell (Uni Cologne). This work has been funded by the Deutsche Forschungsgemeinschaft (DFG, German Research Foundation) within the project "ArctiC Amplification: Climate Relevant Atmospheric and SurfaCe Processes, and Feedback Mechanisms (AC)[3]" as Transregional Collaborative Research Center (TRR) 172, Project-ID 268020496. Luca Lelli, as visiting scientist within the NASA/Goddard Space Flight Center PACE (Plankton, Aerosol, Cloud, ocean Ecosystem) project, is supported by the Alexander von Humboldt Foundation through the Feodor-Lynen Fellowship 2020. Prof. Zhanqing Li (UMD - University of Maryland), Jeremy Werdell (OEL - Ocean Ecology Laboratory,
550 NASA/GSFC) and Andrew Sayer (NASA/GSFC and USRA - Universities Space Research Association) have been instrumental in the establishment of this cooperation. Luca Lelli thanks Theofanis Stamoulis for the initial steps with reflectances, which eventually evolved in this paper.

References

Arosio, C., Rozanov, A., Malinina, E., Weber, M., and Burrows, J. P.: Merging of ozone profiles from SCIAMACHY, OMPS and SAGE II observations to study stratospheric ozone changes, Atmospheric Measurement Techniques, 12, 2423–2444, https://doi.org/10.5194/amt-12-2423-2019, 2019.

Arrhenius, S.: XXXI. On the influence of carbonic acid in the air upon the temperature of the ground, The London, Edinburgh, and Dublin Philosophical Magazine and Journal of Science, 41, 237–276, 1896.

Baldridge, A., Hook, S., Grove, C., and Rivera, G.: The ASTER spectral library version 2.0, Remote Sensing of Environment, 113, 711 – 715, https://doi.org/https://doi.org/10.1016/j.rse.2008.11.007, 2009.

Bennartz, R., Shupe, M., Turner, D., Walden, V., Steffen K., Cox, C., Kulie, M., Miller, N., and Pettersen, C.: Greenland melt extent enhanced by low-level liquid clouds, Nature, https://doi.org/10.1038/nature12002, 2013.

Bjordal, J., Storelvmo, T., Alterskjær, K., and Carlsen, T.: Equilibrium climate sensitivity above 5 C plausible due to state-dependent cloud feedback, Nature Geoscience, 13, 718–721, 2020.

Boccolari, M. and Parmiggiani, F.: Trends and variability of cloud fraction cover in the Arctic, 1982–2009, Theoretical and Applied Climatology, 132, 739–749, https://doi.org/10.1007/s00704-017-2125-6, 2018.

Boisvert, L. N. and Stroeve, J. C.: The Arctic is becoming warmer and wetter as revealed by the Atmospheric Infrared Sounder, Geophysical Research Letters, 42, 4439–4446, https://doi.org/https://doi.org/10.1002/2015GL063775, 2015.

Burrows, J., Hölzle, E., Goede, A., Visser, H., and Fricker, W.: SCIAMACHY, Scanning Imaging Absorption spectroMeter for Atmospheric CHartographY, Acta Astronautica, 35, 445 – 451, https://doi.org/https://doi.org/10.1016/0094-5765(94)00278-T, earth Observation, 1995.

Burrows, J. P., Weber, M., Buchwitz, M., Rozanov, V., Ladstätter-Weissenmayer, A., Richter, A., DeBeek, R., Hoogen, R., Bramstedt, K., Eichmann, K.-U., Eisinger, M., and Perner, D.: The Global Ozone Monitoring Experiment (GOME): Mission Concept and First Scientific Results, Journal of the Atmospheric Sciences, 56, 151–175, https://doi.org/10.1175/1520-0469(1999)056<0151:TGOMEG>2.0.CO;2, 1999.

Chan, M. A. and Comiso, J. C.: Arctic Cloud Characteristics as Derived from MODIS, CALIPSO, and CloudSat, Journal of Climate, 26, 3285–3306, https://doi.org/10.1175/JCLI-D-12-00204.1, 2013.

Clementson, L. A. and Wojtasiewicz, B.: Dataset on the absorption characteristics of extracted phytoplankton pigments, Data in Brief, 24, 103 875, https://doi.org/https://doi.org/10.1016/j.dib.2019.103875, 2019.

Coldewey-Egbers, M., Weber, M., Lamsal, L. N., de Beek, R., Buchwitz, M., and Burrows, J. P.: Total ozone retrieval from GOME UV spectral data using the weighting function DOAS approach, Atmospheric Chemistry and Physics, 5, 1015–1025, https://doi.org/10.5194/acp-5-1015-2005, 2005.

Crook, J. A., Forster, P. M., and Stuber, N.: Spatial patterns of modeled climate feedback and contributions to temperature response and polar amplification, Journal of Climate, 24, 3575–3592, 2011.

Curry, J. A., Schramm, J. L., Rossow, W. B., and Randall, D.: Overview of Arctic cloud and radiation characteristics, Journal of Climate, 9, 1731–1764, 1996.

Delanoë, J. and Hogan, R. J.: Combined CloudSat-CALIPSO-MODIS retrievals of the properties of ice clouds, Journal of Geophysical Research: Atmospheres, 115, https://doi.org/10.1029/2009JD012346, 2010.

Donohoe, A. and Battisti, D. S.: Atmospheric and Surface Contributions to Planetary Albedo, Journal of Climate, 24, 4402–4418, https://doi.org/10.1175/2011JCLI3946.1, 2011.

590 Eastman, R. and Warren, S. G.: Interannual Variations of Arctic Cloud Types in Relation to Sea Ice, Journal of Climate, 23, 4216–4232, https://doi.org/10.1175/2010JCLI3492.1, 2010a.

Eastman, R. and Warren, S. G.: Arctic Cloud Changes from Surface and Satellite Observations, Journal of Climate, 23, 4233–4242, https://doi.org/10.1175/2010JCLI3544.1, 2010b.

Ebell, K., Nomokonova, T., Maturilli, M., and Ritter, C.: Radiative Effect of Clouds at Ny-Ålesund, Svalbard, as Inferred from Ground-Based
595 Remote Sensing Observations, Journal of Applied Meteorology and Climatology, 59, 3–22, https://doi.org/10.1175/JAMC-D-19-0080.1, 2019.

Efron, B. and Tibshirani, R. J.: An Introduction to the Bootstrap, Chapman & Hall, New York, 1993.

Fazel-Rastgar, F.: Seasonal Analysis of Atmospheric Changes in Hudson Bay during 1998-2018, American Journal of Climate Change, 9, 100, https://doi.org/10.4236/ajcc.2020.92008, 2020.

600 Flittner, D. E., Bhartia, P. K., and Herman, B. M.: O_3 profiles retrieved from limb scatter measurements: Theory, Geophysical Research Letters, 27, 2601–2604, https://doi.org/10.1029/1999GL011343, 2000.

Francis, J. A. and Hunter, E.: New insight into the disappearing Arctic sea ice, Eos, Transactions American Geophysical Union, 87, 509–511, https://doi.org/10.1029/2006EO460001, 2006.

Frey, K. E., Comiso, J., Cooper, L. W., Grebmeier, J. M., and Stock, L. V.: Arctic Ocean primary productivity: The response of marine algae
605 to climate warming and sea ice decline, in: Arctic Report Card, vol. 100, NOAA, https://www.arctic.noaa.gov/Report-Card, 2018.

Gaudel, A., Cooper, O. R., Chang, K.-L., Bourgeois, I., Ziemke, J. R., Strode, S. A., Oman, L. D., Sellitto, P., Nédélec, P., Blot, R., Thouret, V., and Granier, C.: Aircraft observations since the 1990s reveal increases of tropospheric ozone at multiple locations across the Northern Hemisphere, Science Advances, 6, https://doi.org/10.1126/sciadv.aba8272, 2020.

Gettelman, A. and Sherwood, S.: Processes responsible for cloud feedback, Current climate change reports, 2, 179–189, 2016.

610 Gettelman, A., Hannay, C., Bacmeister, J. T., Neale, R. B., Pendergrass, A. G., Danabasoglu, G., Lamarque, J.-F., Fasullo, J. T., Bailey, D. A., Lawrence, D. M., and Mills, M. J.: High Climate Sensitivity in the Community Earth System Model Version 2 (CESM2), Geophysical Research Letters, 46, 8329–8337, https://doi.org/https://doi.org/10.1029/2019GL083978, 2019.

Gorshelev, V., Serdyuchenko, A., Weber, M., Chehade, W., and Burrows, J. P.: High spectral resolution ozone absorption cross-sections. Part 1: Measurements, data analysis and comparison with previous measurements around 293 K, Atmospheric Measurement Techniques, 7,
615 609–624, https://doi.org/10.5194/amt-7-609-2014, 2014.

Graßl, S. and Ritter, C.: Properties of Arctic Aerosol Based on Sun Photometer Long-Term Measurements in Ny-Ålesund, Svalbard, Remote Sensing, 11, https://doi.org/10.3390/rs11111362, 2019.

Grosvenor, D. P., Sourdeval, O., Zuidema, P., Ackerman, A., Alexandrov, M. D., Bennartz, R., Boers, R., Cairns, B., Chiu, J. C., Christensen, M., et al.: Remote sensing of droplet number concentration in warm clouds: A review of the current state of knowledge and perspectives,
620 Reviews of Geophysics, 56, 409–453, 2018.

Guarino, M.-V., Sime, L. C., Schröeder, D., Malmierca-Vallet, I., Rosenblum, E., Ringer, M., Ridley, J., Feltham, D., Bitz, C., Steig, E. J., et al.: Sea-ice-free Arctic during the Last Interglacial supports fast future loss, Nature Climate Change, 10, 928–932, 2020.

He, M., Hu, Y., Chen, N., Wang, D., Huang, J., and Stamnes, K.: High cloud coverage over melted areas dominates the impact of clouds on the albedo feedback in the Arctic, Scientific Reports, 9, https://doi.org/10.1038/s41598-019-44155-w, 2019.

625 Herman, G. and Goody, R.: Formation and persistence of summertime Arctic stratus clouds, Journal of the Atmospheric Sciences, 33, 1537–1553, 1976.

Hilboll, A., Richter, A., and Burrows, J. P.: Long-term changes of tropospheric NO_2 over megacities derived from multiple satellite instruments, Atmospheric Chemistry and Physics, 13, 4145–4169, https://doi.org/10.5194/acp-13-4145-2013, 2013.

Hofer, S., Tedstone, A. J., Fettweis, X., and Bamber, J. L.: Decreasing cloud cover drives the recent mass loss on the Greenland Ice Sheet,
630   Science Advances, 3, https://doi.org/10.1126/sciadv.1700584, 2017.

Hofer, S., Tedstone, A. J., Fettweis, X., and Bamber, J. L.: Cloud microphysics and circulation anomalies control differences in future Greenland melt, Nature Climate Change, 9, 523–528, https://doi.org/10.1038/s41558-019-0507-8, 2019.

Holland, M. M., Bitz, C. M., Tremblay, B., Bailey, D. A., et al.: The role of natural versus forced change in future rapid summer Arctic ice loss, Arctic Sea Ice Decline: Observations, Projections, Mechanisms, and Implications, Geophys. Monogr. Ser, 180, 133–150, 2008.

635 Intrieri, J. M., Fairall, C. W., Shupe, M. D., Persson, P. O. G., Andreas, E. L., Guest, P. S., and Moritz, R. E.: An annual cycle of Arctic surface cloud forcing at SHEBA, Journal of Geophysical Research: Oceans, 107, SHE 13–1–SHE 13–14, https://doi.org/https://doi.org/10.1029/2000JC000439, 2002.

Istomina, L., Nicolaus, M., and Perovich, D. K.: Spectral albedo of sea ice and melt ponds measured during POLARSTERN cruise ARK-XXVII/3 (IceArc) in 2012, https://doi.org/10.1594/PANGAEA.815111, 2013.

640 Jones, P. W.: First-and second-order conservative remapping schemes for grids in spherical coordinates, Monthly Weather Review, 127, 2204–2210, 1999.

Kapsch, M.-L., Graversen, R. G., and Tjernström, M.: Springtime atmospheric energy transport and the control of Arctic summer sea-ice extent, Nature Climate Change, 3, 744–748, https://doi.org/10.1038/NCLIMATE1884, 2013.

Karlsson, K.-G. and Devasthale, A.: Inter-comparison and evaluation of the four longest satellite-derived cloud climate data records: CLARA-
645   A2, ESA Cloud CCI V3, ISCCP-HGM, and PATMOS-x, Remote Sensing, 10, 1567, https://doi.org/10.3390/rs10101567, 2018.

Kay, J. E. and L'Ecuyer, T.: Observational constraints on Arctic Ocean clouds and radiative fluxes during the early 21st century, Journal of Geophysical Research: Atmospheres, 118, 7219–7236, https://doi.org/10.1002/jgrd.50489, 2013.

King, N. and Vaughan, G.: Using passive remote sensing to retrieve the vertical variation of cloud droplet size in marine stratocumulus: An assessment of information content and the potential for improved retrievals from hyperspectral measurements, Journal of Geophysical
650   Research: Atmospheres, 117, 2012.

Kokhanovsky, A. and Rozanov, V. V.: Droplet vertical sizing in warm clouds using passive optical measurements from a satellite, Atmospheric Measurement Techniques, 5, 517–528, https://doi.org/10.5194/amt-5-517-2012, 2012.

Kokhanovsky, A. and Tomasi, C.: Physics and Chemistry of the Arctic Atmosphere, Springer, 2020.

Krijger, J. M., van Weele, M., Aben, I., and Frey, R.: Technical Note: The effect of sensor resolution on the number of cloud-free observations
655   from space, Atmospheric Chemistry and Physics, 7, 2881–2891, https://doi.org/10.5194/acp-7-2881-2007, 2007.

Lelli, L. and Vountas, M.: Chapter 5 - Aerosol and Cloud Bottom Altitude Covariations From Multisensor Spaceborne Measurements, in: Remote Sensing of Aerosols, Clouds, and Precipitation, edited by Islam, T., Hu, Y., Kokhanovsky, A., and Wang, J., pp. 109–127, Elsevier, https://doi.org/https://doi.org/10.1016/B978-0-12-810437-8.00005-0, 2018.

Lelli, L., Kokhanovsky, A. A., Rozanov, V. V., Vountas, M., Sayer, A. M., and Burrows, J. P.: Seven years of global retrieval of cloud
660   properties using space-borne data of GOME, Atmospheric Measurement Techniques, 5, 1551–1570, https://doi.org/10.5194/amt-5-1551-2012, 2012.

Lelli, L., Kokhanovsky, A. A., Rozanov, V. V., Vountas, M., and Burrows, J. P.: Linear trends in cloud top height from passive observations in the oxygen A-band, Atmospheric Chemistry and Physics, 14, 5679–5692, https://doi.org/10.5194/acp-14-5679-2014, 2014.

Letterly, A., Key, J., and Liu, Y.: Arctic climate: changes in sea ice extent outweigh changes in snow cover, The Cryosphere, 12, 3373–3382,
665   https://doi.org/10.5194/tc-12-3373-2018, 2018.

Li, Z. and Leighton, H. G.: Scene identification and its effect on cloud radiative forcing in the Arctic, Journal of Geophysical Research:
    Atmospheres, 96, 9175–9188, https://doi.org/https://doi.org/10.1029/91JD00529, 1991.

Lindsay, R. and Zhang, J.: The thinning of Arctic sea ice, 1988–2003: Have we passed a tipping point?, Journal of Climate, 18, 4879–4894,
    2005.

670   Linlu, M., Burrows, J. P., Zhao, X., Vountas, M., Rozanov, V., Lelli, L., Li, X., Guo, H., Nakoudi, K., Ritter, C., and Edebor, A. A.: An
    analysis of AOT above the ocean in the Arctic observed from space: a reducing trend from 1981 to 2020, to be submitted, 2021.

Lohmann, U.: A glaciation indirect aerosol effect caused by soot aerosols, Geophysical Research Letters, 29, 11–1–11–4,
    https://doi.org/https://doi.org/10.1029/2001GL014357, 2002.

Lohmann, U., Tselioudis, G., and Tyler, C.: Why is the cloud albedo–particle size relationship different in optically thick and optically thin
675   clouds?, Geophysical research letters, 27, 1099–1102, 2000.

Matus, A. V. and L'Ecuyer, T. S.: The role of cloud phase in Earth's radiation budget, Journal of Geophysical Research: Atmospheres, 122,
    2559–2578, https://doi.org/https://doi.org/10.1002/2016JD025951, 2017.

McCrystall, M. R., Stroeve, J., Serreze, M., Forbes, B. C., and Screen, J. A.: New climate models reveal faster and larger increases in Arctic
    precipitation than previously projected, Nature Communications, 12, 1–12, https://doi.org/10.1038/s41467-021-27031-y, 2021.

680   Meerdink, S. K., Hook, S. J., Roberts, D. A., and Abbott, E. A.: The ECOSTRESS spectral library version 1.0, Remote Sensing of Environ-
    ment, 230, 111 196, https://doi.org/https://doi.org/10.1016/j.rse.2019.05.015, 2019.

Mieruch, S.: Identification and statistical analysis of global water vapour trends based on satellite data, Ph.D. thesis, University of Bremen,
    http://nbn-resolving.de/urn:nbn:de:gbv:46-diss000115889, 2009.

Morrison, A. L., Kay, J. E., Frey, W. R., Chepfer, H., and Guzman, R.: Cloud Response to Arctic Sea Ice Loss and Impli-
685   cations for Future Feedback in the CESM1 Climate Model, Journal of Geophysical Research: Atmospheres, 124, 1003–1020,
    https://doi.org/10.1029/2018JD029142, 2019.

Mudelsee, M.: Climate Time Series Analysis: Classical Statistical and Bootstrap Methods, Atmospheric and Oceanographic Sciences Library,
    Vol. 42, Springer, Dordrecht Heidelberg London New York, https://doi.org/10.1007/978-90-481-9482-7, 2010.

Munro, R., Lang, R., Klaes, D., Poli, G., Retscher, C., Lindstrot, R., Huckle, R., Lacan, A., Grzegorski, M., Holdak, A., Kokhanovsky, A.,
690   Livschitz, J., and Eisinger, M.: The GOME-2 instrument on the Metop series of satellites: instrument design, calibration, and level 1 data
    processing – an overview, Atmospheric Measurement Techniques, 9, 1279–1301, https://doi.org/10.5194/amt-9-1279-2016, 2016.

Onarheim, I. H., Eldevik, T., Smedsrud, L. H., and Stroeve, J. C.: Seasonal and regional manifestation of Arctic sea ice loss, Journal of
    Climate, 31, 4917–4932, 2018.

Philipp, D., Stengel, M., and Ahrens, B.: Analyzing the Arctic Feedback Mechanism between Sea Ice and Low-Level Clouds Using 34 Years
695   of Satellite Observation, Journal of Climate, 33, 7479 – 7501, https://doi.org/10.1175/JCLI-D-19-0895.1, 2020.

Pistone, K., Eisenman, I., and Ramanathan, V.: Observational determination of albedo decrease caused by vanishing Arctic sea ice, Proceed-
    ings of the National Academy of Sciences, 111, 3322–3326, https://doi.org/10.1073/pnas.1318201111, 2014.

Pithan, F. and Mauritsen, T.: Arctic amplification dominated by temperature feedbacks in contemporary climate models, Nature Geoscience,
    7, 181, 2014.

700   Platnick, S.: Vertical photon transport in cloud remote sensing problems, Journal of Geophysical Research: Atmospheres, 105, 22 919–22 935,
    https://doi.org/10.1029/2000JD900333, 2000.

Rinke, A., Segger, B., Crewell, S., Maturilli, M., Naakka, T., Nygård, T., Vihma, T., Alshawaf, F., Dick, G., Wickert, J., et al.: Trends of vertically integrated water vapor over the Arctic during 1979–2016: Consistent moistening all over?, Journal of Climate, 32, 6097–6116, https://doi.org/10.1175/JCLI-D-19-0092.1, 2019.

705 Rozanov, V. V. and Kokhanovsky, A. A.: Semianalytical cloud retrieval algorithm as applied to the cloud top altitude and the cloud geometrical thickness determination from top-of-atmosphere reflectance measurements in the oxygen A band, Journal of Geophysical Research: Atmospheres, 109, https://doi.org/https://doi.org/10.1029/2003JD004104, 2004.

Schlundt, C., Kokhanovsky, A. A., Rozanov, V. V., and Burrows, J. P.: Determination of cloud optical thickness over snow using satellite measurements in the oxygen A-Band, IEEE Geoscience and Remote Sensing Letters, 10, 1162–1166, 2013.

710 Schmale, J., Zieger, P., and Ekman, A. M.: Aerosols in current and future Arctic climate, Nature Climate Change, pp. 1–11, 2021.

Schweiger, A. J.: Changes in seasonal cloud cover over the Arctic seas from satellite and surface observations, Geophysical Research Letters, 31, https://doi.org/10.1029/2004GL020067, 2004.

Screen, J. A. and Simmonds, I.: The central role of diminishing sea ice in recent Arctic temperature amplification, Nature, 464, 1334–1337, https://doi.org/10.1038/nature09051, 2010.

715 Serreze, M. C. and Barry, R. G.: Processes and impacts of Arctic amplification: A research synthesis, Global and Planetary Change, 77, 85–96, https://doi.org/https://doi.org/10.1016/j.gloplacha.2011.03.004, 2011.

Serreze, M. C. and Barry, R. G.: The Arctic Climate System, Cambridge Atmospheric and Space Science Series, Cambridge University Press, 2 edn., https://doi.org/10.1017/CBO9781139583817, 2014.

Serreze, M. C. and Francis, J. A.: The Arctic amplification debate, Climatic change, 76, 241–264, 2006.

720 Shahi, S., Abermann, J., Heinrich, G., Prinz, R., and Schöner, W.: Regional Variability and Trends of Temperature Inversions in Greenland, Journal of Climate, 33, 9391 – 9407, https://doi.org/10.1175/JCLI-D-19-0962.1, 2020.

Shupe, M. D. and Intrieri, J. M.: Cloud radiative forcing of the Arctic surface: The influence of cloud properties, surface albedo, and solar zenith angle, Journal of Climate, 17, 616–628, https://doi.org/10.1175/1520-0442(2004)017<0616:CRFOTA>2.0.CO;2, 2004.

Shupe, M. D., Rex, M., Dethloff, K., Damm, E., Fong, A. A., Gradinger, R., Heuze, C., Loose, B., Makarov, A., Maslowski, W., Nicolaus, 725 M., Perovich, D., Rabe, B., Rinke, A., Sokolov, V., and Sommerfeld, A.: The MOSAiC Expedition: A Year Drifting with the Arctic Sea Ice, Arctic report card, https://doi.org/10.25923/9g3v-xh92, 2021.

Sledd, A. and L'Ecuyer, T.: How Much Do Clouds Mask the Impacts of Arctic Sea Ice and Snow Cover Variations? Different Perspectives from Observations and Reanalyses, Atmosphere, 10, 12, https://doi.org/10.3390/atmos10010012, 2019.

Smith, A., Jahn, A., and Wang, M.: Seasonal transition dates can reveal biases in Arctic sea ice simulations, The Cryosphere, 14, 2977–2997, 730 https://doi.org/10.5194/tc-14-2977-2020, 2020.

Stengel, M., Mieruch, S., Jerg, M., Karlsson, K.-G., Scheirer, R., Maddux, B., Meirink, J., Poulsen, C., Siddans, R., Walther, A., and Hollmann, R.: The Clouds Climate Change Initiative: Assessment of state-of-the-art cloud property retrieval schemes applied to AVHRR heritage measurements, Remote Sensing of Environment, 162, 363 – 379, https://doi.org/https://doi.org/10.1016/j.rse.2013.10.035, 2015.

Stengel, M., Stapelberg, S., Sus, O., Schlundt, C., Poulsen, C., Thomas, G., Christensen, M., Carbajal Henken, C., Preusker, R., Fischer, 735 J., Devasthale, A., Willén, U., Karlsson, K.-G., McGarragh, G. R., Proud, S., Povey, A. C., Grainger, R. G., Meirink, J. F., Feofilov, A., Bennartz, R., Bojanowski, J. S., and Hollmann, R.: Cloud property datasets retrieved from AVHRR, MODIS, AATSR and MERIS in the framework of the Cloud_cci project, Earth System Science Data, 9, 881–904, https://doi.org/10.5194/essd-9-881-2017, 2017.

Stengel, M., Stapelberg, S., Sus, O., Finkensieper, S., Würzler, B., Philipp, D., Hollmann, R., Poulsen, C., Christensen, M., and McGarragh, G.: Cloud_cci Advanced Very High Resolution Radiometer post meridiem (AVHRR-PM) dataset version 3: 35-year climatology of global cloud and radiation properties, Earth System Science Data, 12, 41–60, https://doi.org/10.5194/essd-12-41-2020, 2020.

Taylor, P. C., Cai, M., Hu, A., Meehl, J., Washington, W., and Zhang, G. J.: A decomposition of feedback contributions to polar warming amplification, Journal of Climate, 26, 7023–7043, 2013.

Tilstra, L. G., de Graaf, M., Aben, I., and Stammes, P.: In-flight degradation correction of SCIAMACHY UV reflectances and Absorbing Aerosol Index, Journal of Geophysical Research: Atmospheres, 117, https://doi.org/10.1029/2011JD016957, 2012.

Tselioudis, G., Rossow, W. B., and Rind, D.: Global patterns of cloud optical thickness variation with temperature, Journal of climate, 5, 1484–1495, 1992.

Turner, J., Comiso, J. C., Marshall, G. J., Lachlan-Cope, T. A., Bracegirdle, T., Maksym, T., Meredith, M. P., Wang, Z., and Orr, A.: Non-annular atmospheric circulation change induced by stratospheric ozone depletion and its role in the recent increase of Antarctic sea ice extent, Geophysical Research Letters, 36, https://doi.org/https://doi.org/10.1029/2009GL037524, 2009.

van Diedenhoven, B., Hasekamp, O. P., and Aben, I.: Surface pressure retrieval from SCIAMACHY measurements in the O_2 A Band: validation of the measurements and sensitivity on aerosols, Atmospheric Chemistry and Physics, 5, 2109–2120, https://doi.org/10.5194/acp-5-2109-2005, 2005.

von Savigny, C., Haley, C. S., Sioris, C. E., McDade, I. C., Llewellyn, E. J., Degenstein, D., Evans, W. F. J., Gattinger, R. L., Griffioen, E., Kyrölä, E., Lloyd, N. D., McConnell, J. C., McLinden, C. A., Mégie, G., Murtagh, D. P., Solheim, B., and Strong, K.: Stratospheric ozone profiles retrieved from limb scattered sunlight radiance spectra measured by the OSIRIS instrument on the Odin satellite, Geophysical Research Letters, 30, https://doi.org/10.1029/2002GL016401, 2003.

Wang, X. and Key, J. R.: Recent trends in Arctic surface, cloud, and radiation properties from space, Science, 299, 1725–1728, https://doi.org/10.1126/science.1078065, 2003.

Wang, X. and Key, J. R.: Arctic Surface, Cloud, and Radiation Properties Based on the AVHRR Polar Pathfinder Dataset. Part I: Spatial and Temporal Characteristics, Journal of Climate, 18, 2558–2574, https://doi.org/10.1175/JCLI3438.1, 2005a.

Wang, X. and Key, J. R.: Arctic Surface, Cloud, and Radiation Properties Based on the AVHRR Polar Pathfinder Dataset. Part II: Recent Trends, Journal of Climate, 18, 2575–2593, https://doi.org/10.1175/JCLI3439.1, 2005b.

Wendisch, M., Macke, A., Ehrlich, A., Lüpkes, C., Mech, M., Chechin, D., Dethloff, K., Velasco, C. B., Bozem, H., Brückner, M., Clemen, H.-C., Crewell, S., Donth, T., Dupuy, R., Ebell, K., Egerer, U., Engelmann, R., Engler, C., Eppers, O., Gehrmann, M., Gong, X., Gottschalk, M., Gourbeyre, C., Griesche, H., Hartmann, J., Hartmann, M., Heinold, B., Herber, A., Herrmann, H., Heygster, G., Hoor, P., Jafariserajehlou, S., Jäkel, E., Järvinen, E., Jourdan, O., Köstner, U., Kecorius, S., Knudsen, E. M., Köllner, F., Kretzschmar, J., Lelli, L., Leroy, D., Maturilli, M., Mei, L., Mertes, S., Mioche, G., Neuber, R., Nicolaus, M., Nomokonova, T., Notholt, J., Palm, M., van Pinxteren, M., Quaas, J., Richter, P., Ruiz-Donoso, E., Schëfer, M., Schmieder, K., Schnaiter, M., Schneider, J., Schwarzenböck, A., Seifert, P., Shupe, M. D., Siebert, H., Spreen, G., Stapf, J., Stratmann, F., Vogl, T., Welti, A., Wex, H., Wiedensohler, A., Zanatta, M., and Zeppenfeld, S.: The Arctic Cloud Puzzle: Using ACLOUD/PASCAL Multiplatform Observations to Unravel the Role of Clouds and Aerosol Particles in Arctic Amplification, Bulletin of the American Meteorological Society, 100, 841 – 871, https://doi.org/10.1175/BAMS-D-18-0072.1, 2019.

Wilks, D. S.: Resampling Hypothesis Tests for Autocorrelated Fields, Journal of Climate, 10, 65–82, https://doi.org/10.1175/1520-0442(1997)010<0065:RHTFAF>2.0.CO;2, 1997.

775 Zelinka, M. D., Myers, T. A., McCoy, D. T., Po-Chedley, S., Caldwell, P. M., Ceppi, P., Klein, S. A., and Taylor, K. E.: Causes of higher climate sensitivity in CMIP6 models, Geophysical Research Letters, 47, e2019GL085 782, 2020.

Zheng, Y., Rosenfeld, D., and Li, Z.: Satellite inference of thermals and cloud-base updraft speeds based on retrieved surface and cloud-base temperatures, Journal of Atmospheric Sciences, 72, 2411–2428, https://doi.org/10.1175/JAS-D-14-0283.1, 2015.

Zygmuntowska, M., Mauritsen, T., Quaas, J., and Kaleschke, L.: Arctic Clouds and Surface Radiation - a critical comparison of satellite
780 retrievals and the ERA-Interim reanalysis, Atmospheric Chemistry and Physics, 12, 6667–6677, https://doi.org/10.5194/acp-12-6667-2012, 2012.